DESIGN AND CONSTRUCTION OF A FORWARD VIEWING, WIDE-FIELD GASTROSCOPE ENDCAP IMAGER

by

Andrea Manjarres Chambas

Thesis Submitted in Partial Fulfillment
of the requirements for the Degree of
Bachelor of Applied Science
in the School of Engineering Science
SIMON FRASER UNIVERSITY

MAY 2020

All rights reserved. This work may not be
reproduced in whole or in part, by photocopy
or other means, without the permission of the author.

APPROVAL

Name: Andrea Manjarres Chambas

Degree: Bachelor of Applied Science (Honours)

Title of Thesis: Design and Construction of a Forward Viewing Wide-Field Gastroscope Endcap Imager

Glenn Chapman

Dr. Glenn Chapman, P.Eng
Director
School of Engineering Science

Examining Committee:

Dr. Anthony Lee (Technical Supervisor and Academic Co-Supervisor)
Staff Scientist
BC Cancer Research Institute

Dr. Pierre Lane (Academic Co-Supervisor and Chair), P.Eng
Associate Professor of Professional Practice, School of Engineering Science
Senior Scientist, BC Cancer Research Institute

MSarunic

Dr. Marinko Sarunic, P.Eng
Professor and Associate Director
School of Engineering Science

Date Approved: July 15-2020

Abstract

Gastric cancer is the third most common cause of cancer-related deaths worldwide [1]. It has a 25% 5-year survival rate, which is most likely due to the fact that 45% of cases are diagnosed in stage IV, when the cancer has already metastasized [2]. It is diagnosed through pathological examination of histological biopsies obtained during gastroscopies. A gastroscopy is a procedure in which a doctor examines the stomach using different imaging modalities, such as white light imaging (WLI) and narrowband imaging (NBI) [3].

In order to increase the diagnostic ability of gastroscopies, an assistive device called a gastroscope endcap imager (GEI) is being proposed. The GEI presents a large field of view (FOV) using the imaging paradigm dual-beam manually actuated distortion-corrected imaging (DMDI) [4, 5]. The proposed GEI will be a multi-modal imaging device that is designed to be attachable to the distal end of a gastroscope, and will provide two imaging modalities, namely optical coherence tomography (OCT) and NBI.

The work covered in this thesis project is the mechanical and optical mechanisms that will be used to develop a GEI prototype. More specifically, a detailed discussion of the simulations, manufacturing processes, experiments, and iterative design processes is presented. It was found that it is feasible to manufacture collimators that can achieve a resolution of ≤ 50 µm, and to mechanically actuate fibers to create stable scans with a FOV of 9 mm.

Acknowledgments

I would like to thank all my supervisors: Anthony, Pierre and Marinko. Specially Anthony, for allowing me to do this work that has lead me to grow and end my degree with the best experience possible.

I also would like to thank everyone in the photonics team in BCCRC. Particularly Geoffrey, Andie and Eric for listening, helping me find solutions, and reading my work.

Lastly, I would to thank my mom, boyfriend and family for letting me rant during those nights in which this goal seemed impossible and for encouraging me to always do my best.

Contents

1 Background **1**

1.1 Gastric Cancer 1

1.2 Endoscopic Imaging Modalities 3

1.2.1 Chromoendoscopy 3

1.2.2 Narrowband imaging 3

1.2.3 Blue laser imaging 4

1.2.4 Linked color imaging 4

1.2.5 Autofluorescence imaging 5

1.2.6 Confocal laser endoscopy 5

1.2.7 Optical Coherence Tomography 5

2 Gastroscope endcap imager **6**

2.1 Clinical Need 6

2.2 Point-scanning mechanisms 7

2.2.1 Side-viewing 7

2.2.2 Forward-viewing 7

2.3 Dual beam manually actuated distortion corrected imaging 8

2.4 GEI overview 9

2.5 Thesis outline 10

3 Optical System **11**

3.1 Overview 11

3.2 Requirements 11

3.3 Light Source Modeling 12

  3.3.1 Background 12

  3.3.2 Point Source 13

3.4 Gaussian Source 13

3.5 Fiber characterization 14

  3.5.1 Collimator Design 14

  3.5.2 Fiber Simulation 15

  3.5.3 Collimator Realization 16

3.6 Beam collimation optimization 17

  3.6.1 Background 17

  3.6.2 Methodology 17

  3.6.3 Results 18

3.7 Resolution 19

  3.7.1 Background 19

  3.7.2 Methodology 19

  3.7.3 Results 20

3.8 Power Loss 20

  3.8.1 Background 20

  3.8.2 Methodology 21

3.8.3 Results 22

3.9 Current State 23

3.10 Future work 24

4 Mechanical System **24**

4.1 Overview 24

4.2 Requirements 25

4.3 Experimental Set-up 27

4.4 Rotor Attachment 28

4.4.1 Background: Motor 28

4.4.2 Design Considerations 29

4.4.3 Printed rotor Attachments 29

4.4.4 Machined rotor attachment 31

4.5 Housing 32

4.5.1 Design Considerations 32

4.5.2 Previous Versions 32

4.5.3 Final testing prototype 33

4.6 Scan Amplitude 36

4.6.1 Background 36

4.6.2 Methodology 36

4.6.3 Results 37

4.7 Scan stability 38

4.7.1 Background 38
4.7.2 Methodology 38
4.7.3 Results 40
4.8 Scan frequency 42
4.8.1 Background 42
4.8.2 Methodology 43
4.8.3 Results 43
4.9 Lifetime 45
4.9.1 Background 45
4.9.2 Methodology 45
4.9.3 Results 45
4.10 Current State 47
4.11 Future Work 48

5 Future Work **48**

5.1 Conclusion 49

List of Figures

1 Stomach Layers and regions [8]. 1
2 Gastric body a) healthy mucosa, honeycomb SECN and CV (in green) are observed, b) mucosa diagnosed with *H. pylori* infection associated gastritis, englarged pits can be seen, c) mucosa with gastritis diagnosed with intestinal metaplasia and d) cancerous lesion, demarcated by yellow arrows [8,13] 2

3 DMDI example a) isometrical view of DMDI equipped galvo scanner, blue and red are the two beams' scan pattern b) Images acquired of QR phantom by the two beams c) Co-registered and corrected images [4] 8

4 GEI overview diagram. a) Diagram of the overall system, including imaging modalities, and interaction of the optical and mechanical systems of the GEI, beam shown in blue. b) Sample images that will be acquired with the NBI and OCT systems, the zigzag pattern represents the scanning pattern of the GEI on the stomach wall. 9

5 Concept drawings of GEI attached to gastroscope. a) front and b) isometric views. The imaging beams used for the DMDI algorithm are shown in red and blue. 10

6 ZEMAX detector at GRIN using point source. 13

7 Sketch used to calculate position (divergence of source), using calculated parameters θ_d and $1/e^2$ radius. 14

8 Optical system design, fiber collimator followed by lens and beam (in red) illustration. 15

9 Experiment Set-up for collimation of beam 17

10 GRIN length vs MMF2 length to collimate beam. 18

11 Spot size at focal plane vs MMF length. 20

12 Power Loss experimental set-up 21

13 Power loss analysis model. Yellow section is power loss. 22

14 Power loss vs MMF length 23

15 Mechanical system conceptual design, a) side view and b) top view. Blue and red lines are the light beams emitted from the collimators. The labeled retaining grooves and pin are part of the rotor attachment. 26

16 Side view of the experimental set-up for frequency experiment. Detector was switched to a camera for the stability experiments. 27

17 System sketch with variables definition 28

18 Motor images a) whole with outer casing removed b) stator and c) rotor. 29

19 First rotor attachment design. 30

20 Second rotor attachment design, a) SOLIDWORKS design, b) 3D printed and polished result. 30

21 Machined rotor attachment a) top view, and b) side view, glued using jig. 31

22 Jig for machined rotor attachments, used 180 degrees rotated in the y-direction but shown this way to ease visibility. 32

23 GEI benchtop housing a) first and b) second iterations (second slit not visible). Slits designed to attach to optical breadboard. Fiber attached to housing using double sided tape. 33

24 Housing third iteration, compatible with optical cage. 33

25 Acceptable testing prototype, compatible with optical cage. 34

26 Final housing version: Fiber Holder 35

27 Scan amplitude: a) measurement diagram and b) sample data. 36

28 Fiber length vs scan amplitude at different l_{p-m}. Points above the required scan amplitude line (pink) meet the requirement; anything below does not. Points labeled with x were not used for curve fitting. 37

29 Minimum l_{fiber} to meet requirement vs l_{p-m}. 38

30 Stability experimental set-up, a) diagram and b) sample scan patterns acquired by camera, using two fibers. 39

31 Stable vs unstable scan comparison a) stable taken with two fibers, b) unstable taken with one fiber. These images were acquired with screenshots of the camera's program. 39

32 Left axis: stability (correlation) vs. fiber length. Right axis: Scan amplitude vs. fiber ratio at two different fiber lengths. 41

33 Stability (correlation) vs. preload with l_{fiber} 24.5 mm, scan amplitude of 9 mm, and a fiber ratio of 1. 42

34 Frequency experimental set-up a) diagram and b) oscilloscope screenshot, from which T_{scan} was recorded for each data point. 43

35 Scan frequency vs motor's operating voltage, point labeled with 'x' were removed because system was unstable. 44

36 Motor's lifetime: frequency against time. 46

37 Fibers' lifetime test: Power output vs time. 47

List of Acronyms

DCF	Dual Clad Fiber
DMDI	Dual-beam Manually-actuated Distortion-Corrected imaging
FOV	Field Of View
FWHM	Full Width Half Max
GEI	Gastroscope Endcap Imager
GRIN	Gradient Index
MEMS	Micro Electrical Mechanical System
MMF	Multimode Fiber
NA	Numerical Aperture
NCF	No Core Fiber
OD	Outer Diameter
RMS	Root Mean Square
RPC	Rotary Pullback Catheter
SMF	Single Mode Fiber
TIR	Total Internal Reflection

1 Background

1.1 Gastric Cancer

Gastric cancer, also known as stomach cancer, is the third most common cause of cancer-related deaths in the world [1]. 3500 Canadians were diagnosed with it in 2017, and 2100 died from it [2]. In Canada, 15% of cases are diagnosed in stage I, and 45% of cases are diagnosed in stage IV, when the cancer has already metastasized [2].

There are numerous sub-types of gastric cancer, however adenocarcinomas are the most common one, being responsible for 95% of cases [6]. Adenocarcinomas begin developing in the inner layer of the stomach wall, and grow to the outer layers as the disease progresses [6]. Thus, imaging of the lumen of the stomach is diagnostically important for early gastric cancer (EGC) detection.

The stomach is a J-shaped organ composed of 4 regions and 4 layers of tissue. From the innermost to the outermost they are: the mucosa, submucosa, muscularis and serosa, as shown in Figure 1. The stomach wall has a thickness that ranges from 2.64 mm to 4.23 mm, within which the mucosa has a thickness that ranges from 1.03 mm to 1.64 mm [7].

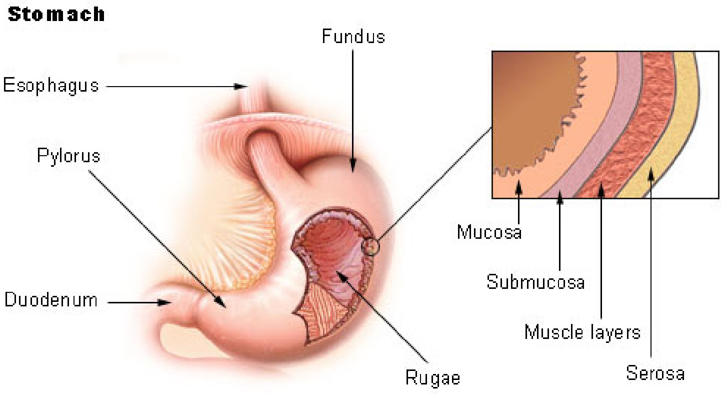

Figure 1: Stomach Layers and regions [8].

The mucosa is covered with small pores called gastric pits that contain exocrine cells that secrete digestive enzymes [9]. In a healthy stomach, shown in Figure 2a, gastric pits have a size of 50 to 70 μm. These are surrounded by sub-epithelial capillary networks (SECN) that have a honeycomb-like shape and are interspersed with spider-like collecting venules (CV) [10–13].

Infection with helicobacter pylori bacteria (*H. pylori*) increases the chances of developing gastric adenocarcinoma six-fold, and is present in two-thirds of the population worldwide [14–16]. The infection causes chronic inflammation of the mucosa (gastritis), the appearance of irregular SECNs, and enlargement and distortion of gastric pits (Figure 2b) [11, 17]. *H. pylori* infection can also lead to pre-malignant conditions such as intestinal metaplasia (IM), atrophic gastritis and dysplasia [18–20]. When IM is present, the cells that normally line the stomach are replaced with cells that are phenotypically similar to the cells that line the intestines. Under endoscopic examination the mucosa appears with an irregular ridge or villous pattern, referred to as light blue crests (LBC) (Figure 2c) [13, 18, 20]. In the case of dysplasia and cancer lesions, the affected areas have a complete loss of mucosal pattern (Figure 2d) [13, 20].

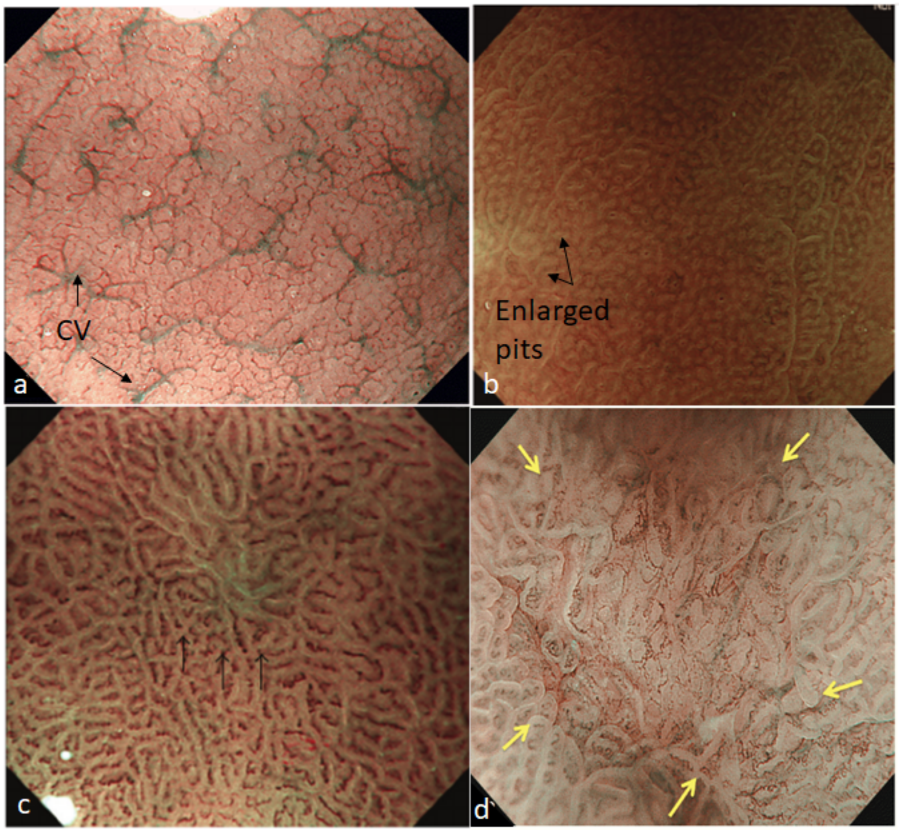

Figure 2: Gastric body a) healthy mucosa, honeycomb SECN and CV (in green) are observed, b) mucosa diagnosed with *H. pylori* infection associated gastritis, englarged pits can be seen, c) mucosa with gastritis diagnosed with intestinal metaplasia and d) cancerous lesion, demarcated by yellow arrows [8, 13]

To diagnose these various stomach conditions, it is important that gastroscopies allow for clinically significant imaging of the underlying microvasculature of the mucosa. In addition, the differentiation and assessment of shallow and deeper blood vessel structures in the mucosal membrane helps physicians to accurately evaluate the nature of gastric lesions [21]. It has also been found that unstructured, scattered vessels are potentially an indicator of sub-mucosal invasion that requires surgical intervention [22]. However, in practice the depth of invasion of lesions is examined by the use of white light imaging (WLI) (described following) and endoscopic ultrasound (EUS) [22].

1.2 Endoscopic Imaging Modalities

The current standard of care technique used in clinical practice for the detection of gastric lesions is WLI [23]. It uses a wide-band of visible light to illuminate the stomach, and can be used with or without magnification [22]. WLI has poor correlation with histopathologic findings, especially when diagnosing *H. pylori* and IM [23–25]. However, it remains a promising technique for the detection of preneoplastic lesions [23]. Magnified WLI has a field of view (FOV) of 213 mm^2 and a maximum resolution of 15 µm [26].

The following techniques are currently being used or studied to augment WLI and improve the early diagnosis of gastric cancer.

1.2.1 Chromoendoscopy

Chromoendoscopy (CE) is an inexpensive diagnostic method in which a chemical dye (usually methylene blue) is sprayed onto the surface of the stomach to highlight morphological differences in the mucosa [24, 25, 27]. After the dye is absorbed, the area is inspected using magnified endoscopy (ME) [25]. Some studies have shown that CE can be more reliable than WLI alone in detecting early lesions of stomach cancer [23, 27]. However, CE is not widely used since it is a time-consuming procedure, and dependent on the skill of the endoscopist [25]. CE has the same maximum resolution and FOV as magnified WLI.

1.2.2 Narrowband imaging

Electronic endoscopic imaging techniques, called virtual CEs, imitate the effects of CE without the need of dyes [28]. One of the most significant virtual CEs for the diagnosis of gastric cancer is narrowband imaging (NBI). It uses optical filters to illuminate the stomach with specific wavelengths, in the blue and green range. NBI is commonly used in combination with ME because the images acquired without magnification in organs with large lumens, such as the stomach, are too dark to see color or structural changes [22].

ME-NBI enhances the mucosal microvasculature and surface patterns to detect small mucosal changes that occur due to various stomach diseases [22]. It has been reported that ME-NBI is more accurate at the surveillance of IM, and has higher sensitivity than WLI when diagnosing premalignant gastric lesions. Additionally, it has a higher diagnostic accuracy for EGC than WLI and CE [22, 29–31]. ME-NBI has also been demonstrated to be a promising method for determining tumor margins [22]. However, ME-NBI prolongs procedure time since it has to be used with magnification, and it requires specialized training [22, 32]. The gastroscope GIF-HQ290 (Olympus) has a ME-NBI FOV of 213 mm^2 and a maximum resolution of 15 µm [26].

ME-NBI uses vasculature information from the mucosa to predict the depth of invasion of a lesion. Some studies have demonstrated that ME-NBI has potential in accurately predicting the invasion depth in EGC. However more studies and guidelines are needed to allow for its application in clinical practice [22].

1.2.3 Blue laser imaging

Blue laser imaging (BLI) is a virtual CE technique that utilizes two lasers with wavelengths of 450 nm and 410 nm and a white light phosphor to enhance vasculature patterns. It has been shown that BLI is more accurate at diagnosing EGC than WLI, and has a higher diagnostic accuracy for IM and chronic gastritis than WLI [21, 33, 34]. BLI, when used in combination with ME, has a similar performance to ME-NBI when diagnosing EGC and *H. pylori* [17, 33, 35]. BLI create brighter images than NBI when both are used without magnification [36]. However, it suffers from some of the same drawbacks as NBI: increases procedure time when used with magnification and requires specialized training [35]. The videoscope LASEREO (Fujifulm), along with light source LL-4450, has a FOV of 213 mm^2 and a resolution of 15 µm [37]. BLI has been known to predict depth of invasion using pit patterns, a small study found that through this method BLI accurately determined the depth of invasion of 13 out of 18 patients (70%) [38].

1.2.4 Linked color imaging

The current state of the art in imaging modalities used in gastroscopies is linked color imaging (LCI). It is a novel technique that uses white light along with narrowband shortwave light and image processing algorithms. It intensifies color contrast of the mucosa, making its images analogous to WLI, so no specialized training is required [35]. It is ideal for usage inside large organs, such as the stomach, because it produces brighter images than WLI and BLI [36]. It is also more effective in the recognition of EGC and *H. pylori* than WLI [35, 39]. The scope EG-760Z (Fujifilm) has a resolution of 1.5 µm and a FOV of 2 mm^2 when used 1.5 mm away from the tissue [40]. Given that LCI is a novel technique, its accuracy in determining the depth of invasion of lesions is yet to be studied [41].

1.2.5 Autofluorescence imaging

Autofluorescence imaging (AFI), consists of using naturally occurring fluorescence to detect cancerous lesions [42]. AFI differentiates between mucosal tissue and neoplastic tissue by comparing their fluorescent properties [23]. Abnormal mucosa shows loss of autoflourescence in comparison to healthy tissue. AFI has a lower sensitivity than WLI to detect neoplastic gastric lesions and it performs particularly poorly when detecting flat neoplastic lesions [23, 43]. The AFI-equipped scope FQ260Z (Olympus) has a maximum resolution of 25 µm, along with a FOV range of 592 mm^2 [44].

1.2.6 Confocal laser endoscopy

Confocal laser endoscopy (CLE), produces cellular resolution images with or without the use of contrast dyes. It has been demonstrated that CLE is superior to WLI in the detection and surveillance of IM [23]. However, CLE has a low tissue penetration of about 250 µm, which stops physicians from visualizing the full mucosal thickness and determining lesions' depth of invasion. CLE has a lateral resolution of 0.7 µm and a FOV of 240 to 600 μm^2, thus it prolongs procedure time significantly when used [23, 45, 46].

1.2.7 Optical Coherence Tomography

Optical coherence tomography (OCT) is an imaging technique that produces high resolution, cross-sectional and three-dimensional images. It is analogous to ultrasound (US), but instead of sound it is based on light-interference and backscattering properties of tissue. It has a tissue depth of penetration (DOP) of a few millimetres (1 mm - 3 mm) and a resolution of a few microns [7, 47–49]. On the other hand, traditional EUS features a DOP of 5 to 6 cm but lower resolution in the range of 0.31 to 0.57 mm depending on the transducer. Such a large DOP is not required to scan the stomach wall since it has a thickness of 2 to 4 mm. [7, 50, 51]. EUS has a FOV of 120 to 180 degrees [52].

OCT works by the use of inteferometers, which have two arms: reference and sample, through which the light from a low-coherence source is split. The light in the reference arm is back-reflected by a reference mirror along the same path it was propagated. The light from the sample arm penetrates the tissue and is backscattered. The light from the two arms then interferes to form A-line scans, which are the intensity of the backscattered signal vs. tissue depth. Multiple A-lines are taken to form 2-D images called B-scans [48].

Studies have shown OCT's potential to increase diagnostic accuracy in the GI tract because of its high resolution, volumetric, and subsurface imaging capabilities [53]. However, most GI tract OCT studies have been performed in the esophagus because the scanning systems are readily available. In the stomach, the largest OCT study involved 5 patients, which determined that OCT is able to identify the differences of gastric pit structure and scattering intensity between sites with IM, dysplasia and cancer [54].

2 Gastroscope endcap imager

2.1 Clinical Need

When performing gastroscopies, the mucosa is scanned without magnification. ME is then used when potential lesions are detected [55]. ME requires physicians to inspect the area 3 mm away from the tissue, which limits the speed of the procedure. This can be problematic when widespread gastritis is present [55]. It is also a common practice to take several non-targeted biopsies because gastritis can mask early lesions. [24, 33, 56, 57]. These non-targeted biopsies only cover a small portion of the total surface area of the stomach, having a high probability of missing small dysplastic lesions [58, 59]. Thus, there is a need for a tool that can more accurately and more quickly guide biopsies, effectively reducing the number of biopsy taken.

Additionally, it is important to keep the instrument channel available to take biopsies. When a tool is put through the instrument channel to scan the stomach, and then needs to be removed once an area of interest is found, there is a possibility of losing the exact biopsy location.

Furthermore, accurately determining the depth of invasion of lesions is important when deciding upon the appropriate treatment for a patient, to lead to a better prognosis. It has been reported that up to 20% of patients do not receive optimal treatment based on the depth of invasion determined with the conventional techniques [22].

The solution proposed in this paper will use NBI along with OCT. NBI was chosen because it effectively differentiates abnormal vasculature from normal, which translates to its good diagnostic ability for *H. pylori*, IM and EGC [23, 29]. However, NBI can extend procedure time because it has to be used with ME, and may miss flat lesions due to limitations in light penetration [53]. Thus, OCT was chosen to complement it. OCT has the ability to image 3-dimensional morphology of the mucosa and gastric pits providing depth invasion information of lesions [4, 5, 53, 60]. Due to its higher resolution, in comparison to EUS, it should more accurately determine the depth of invasion of a lesion, leading to better prognosis.

2.2 Point-scanning mechanisms

There are two main challenges when scanning the mucosa: conforming to the shape of the stomach, and acquiring a large FOV to efficiently scan the stomach. Given that the GEI will use OCT, it is important to discuss the multiple two-dimensional OCT point-scanning mechanisms that have been developed and how they address these challenges.

2.2.1 Side-viewing

Side-viewing mechanisms, as the name suggest, acquire images sideways. They are commonly used in tubular structures, such as the esophagus, trachea, bronchi, veins and arteries. An example of these mechanisms is a rotary pullback catheter (RPC). RPCs acquire two dimensional images by rotating and translating along the same axis. They can achieve large FOVs of up to 225 mm^2, which makes them efficient in scanning large surface areas [61]. However, RPCs have difficulty conforming to highly curved surfaces such as the stomach and they cannot be guided easily by the gastroscope. They are also not well suited to large luminal diameters; if placed against the mucosa they only scan the mucosa for a short area of their FOV [4, 5, 62].

2.2.2 Forward-viewing

Forward-viewing mechanisms have been extensively used to scan the stomach. Some examples of these mechanisms include MEMS and piezotube actuated scanners. These mechanisms are easily guided by the gastroscope and can conform to the shape of the stomach. However, they have small FOVs. For instance, MEMS mirror activated scanners have been reported to achieve a FOV of 2.9 mm x 2.8 mm, and are also expensive [63, 64]. Piezotube forward scanners, have been reported to have a FOV of 2.2 mm x 2.1 mm [65]. Some of these forward-viewing scanners have been designed to work inside the instrument channel of endoscopes, which can limit their maximum FOV and hinder biopsies [63, 65]. Other forward-viewing scanning mechanisms have been designed as hand-held devices but still have a small FOV (i.e.: 4 mm x 1.2 mm) [64]. Such small FOVs make the available forward-viewing scanners inefficient at scanning the mucosa. Thus, none of the available mechanisms can efficiently scan the stomach.

2.3 Dual beam manually actuated distortion corrected imaging

Dual beam manually actuated distortion corrected imaging (DMDI) is an imaging paradigm, to be used with point-scanning mechanisms, that allows for a theoretically infinite FOV and distortion-corrected scans. To achieve these capabilities, DMDI uses two beams, which are mechanically scanned along one direction (fast axis), and spatially separated along the orthogonal direction (slow axis). Both beams scan the same sample features at different times. Since the spatial separation between the beams is known at all times, the time interval between the two beams imaging the same feature can be used to calculate the average scan velocity, allowing for the reconstruction of an undistorted image. A DMDI-capable galvo scanner and sample distorted and distortion-corrected images can be seen in Figure 3 [4, 5].

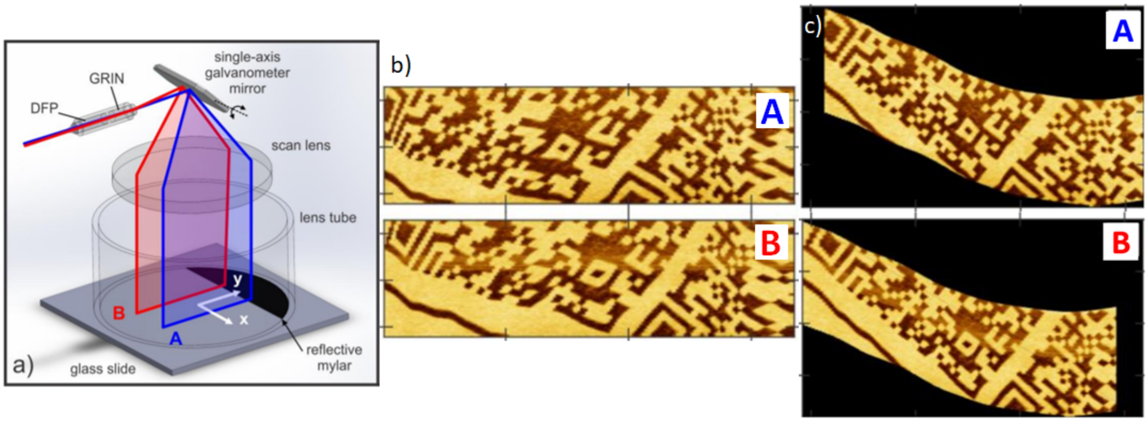

Figure 3: DMDI example a) isometrical view of DMDI equipped galvo scanner, blue and red are the two beams' scan pattern b) Images acquired of QR phantom by the two beams c) Co-registered and corrected images [4]

2.4 GEI overview

The gastroscope endcap imager (GEI) will be a forward-viewing point-scanning mechanism that will be used in gastroscopies to scan the inner layers of the stomach. It will be designed to be attached to the distal end of the gastroscope, such that it does not obstruct the endoscope's video or instrument channel, preventing the hindrance of biopsy collection.

The GEI will use the imaging modalities OCT and NBI. The OCT system will use a 23 mW, 100 kHz, 1310 nm swept-source laser (AXP50125-6, Axsun Technologies, Billerica, MA), whereas the NBI system will use blue and green lasers of 450 and 520 nm respectively [66]. The GEI will allow for the two imaging modalities to be used simultaneously, so that diagnostically relevant information from both modalities can be used jointly to better assess lesions.

The optical system of the GEI will consist of two fiber collimators that will be mechanically scanned behind a lens (f = 12 mm). The mechanical system of the GEI will consist of a DC motor with a custom-made attachment that will mechanically scan the fiber collimators behind the lens (Figure 4a).

The GEI, once attached to the gastroscope, will acquire images with large 2-dimensional FOVs by scanning the stomach wall following a zigzag pattern, as seen in Figure 4b. It will also combine the imaging paradigm DMDI with a large scan amplitude of the fiber collimators. The imaging paradigm DMDI will be used to correct both dimensions from motion artifacts and overlap that may occur while scanning.

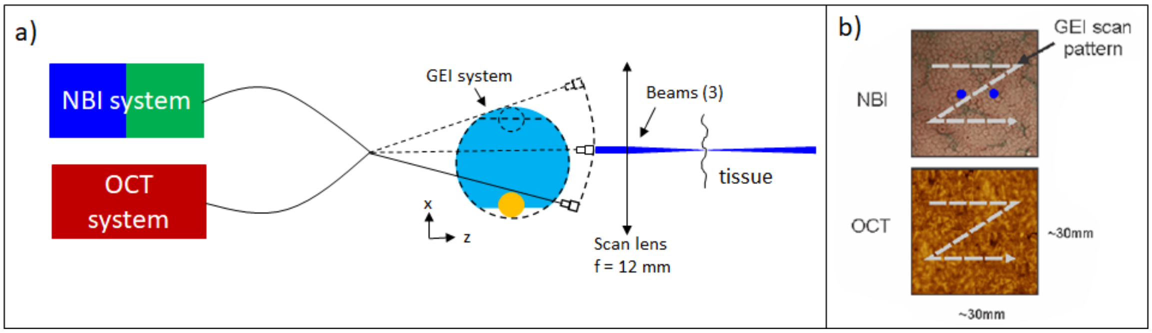

Figure 4: GEI overview diagram. a) Diagram of the overall system, including imaging modalities, and interaction of the optical and mechanical systems of the GEI, beam shown in blue. b) Sample images that will be acquired with the NBI and OCT systems, the zigzag pattern represents the scanning pattern of the GEI on the stomach wall.

In Figure 5 the details of the GEI system can be observed. The GEI will be inside an endcap to securely encapsulate and attach the scanning mechanism to the gastroscope.

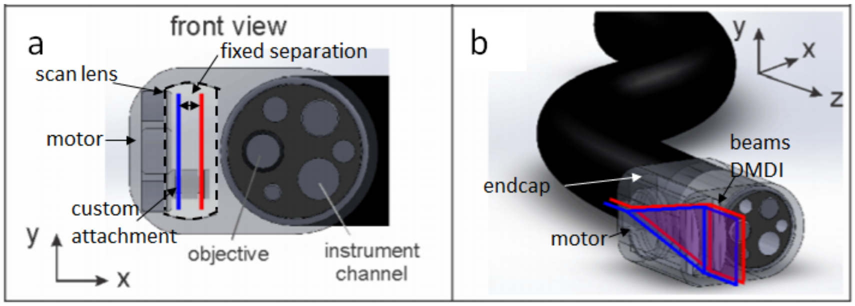

Figure 5: Concept drawings of GEI attached to gastroscope. a) front and b) isometric views. The imaging beams used for the DMDI algorithm are shown in red and blue.

The endcap will have one opening to hold the scanning lens in place and a second opening to secure the GEI to the gastroscope. The scanning lens, will be rectangular and custom ordered with dimensions of 3 mm by 9 mm to reduce the cross-sectional area of the GEI. The optical fibers and actuator mechanism will be inside a semi-flexible umbilical cord and tethered alongside the gastroscope. The materials that will be used to build the GEI will be inexpensive, making it commercially viable as a disposable device.

Furthermore, the GEI has also been designed to have a resolution high enough to resolve gastric pits and irregular microvascular patterns, which will be useful in diagnosing *H. pylori* infection, IM, dysplasia and EGC [11,18,20]. It will also allow for faster scanning of the mucosa by allowing physicians to scan the mucosa 12 mm away from the tissue while conserving a similar resolution to ME.

The ultimate goal of the GEI is to reduce the number of biopsy sites, reduce the rate of missed diagnosis, and increase the detection of early stage gastric cancer.

2.5 Thesis outline

This thesis project was concerned with the development of the fundamental tools and systems necessary for developing a working prototype of the GEI. It was divided into two chapters: optical and mechanical systems. The optical system chapter consisted of designing and determining the ideal parameters for the fiber optic collimators of the GEI. The mechanical system chapter consisted of designing and developing the system that provides linear scanning fibers.

Proceeding the two chapters, there will be an outline of what can be done to improve the systems and next steps, following this work, that will be taken to develop a working prototype of the GEI.

3 Optical System

3.1 Overview

The optical system of the GEI defines what features of the stomach's morphology will be visible. The two main factors taken into account for its design were lateral resolution and power loss. The optical system will consist of two fiber collimators that will be focused onto the tissue using a lens. The scans acquired by the optical system will be processed using DMDI, allowing for distortion corrected images with a large FOV.

The majority of the work done for the optical system was done through simulations, in the optical simulation software ZEMAX v 18.9. The research results that will be discussed in this chapter are:

1. **Light source modeling**, which ensured light in the simulation behaved as in reality.
2. **Fiber characterization**, which determined the fiber parameters needed for the optical simulations.
3. **Beam collimation optimization**, in which the fiber parameters required to collimate the beams were determined.
4. **Resolution**, which established the collimator parameters that could achieve the required resolution.
5. **Power loss**, which determined the collimator parameters that had an acceptable power loss.

3.2 Requirements

The optical system of the GEI has been designed to meet the following requirements:

1. **Resolution**

   The main requirement of the GEI's optical system is the ability to resolve gastric pits, for the following two reasons: firstly, irregular shaped gastric pits are an indicator of dysplastic changes [13]. Secondly, if gastric pits are resolvable then they may be useful for DMDI image coregistration. Therefore, the full width half max (FWHM) of the beams emitted from the GEI is required to be ≤ 50 µm, which is the smallest gastric pit size reported in literature [10].

2. **Power Loss**

   To minimize noise caused by scattering of lost light (non-collimated light) the total power loss from the fiber optic system was compared to the power loss that occurs in an optical splice, which is -0.05 dB [67].

Lastly, a summary of the current state of the optical system, its characteristics and future work will be presented.

3.3 Light Source Modeling

3.3.1 Background

For the simulations it was necessary to use a light source that would imitate the behaviour of light as it is emitted from the fibers used for the collimators. Therefore, the light source in the simulations needed to have the same numerical aperture (NA) as the fibers in reality. The acceptance angle of the fibers was found using Equation 1:

$$\theta_a = sin^{-1}(NA) \tag{1}$$

where θ_a is the acceptance angle, which is also the angle at which the light diverges into free space as it leaves the fiber. The fibers to be used in the GEI are a dual clad fiber (DCF) (SM-9/105/125-20A Nufern Inc., East Granby, CT) with a core NA of 0.12, and a single mode fiber (SMF) (SMF-28, Thorlabs Inc., Newton, NJ) with a core NA of 0.14. Using these values, the acceptance angles for the DCF and SMF were found to be 6.7 degrees and 8.0 degrees.

For the simulations of the GEI there were mainly two ZEMAX light sources that were experimented with.

3.3.2 Point Source

Through the initial simulations, a point light source was used. The point source is defined in ZEMAX's documentation as a point that emits rays into a cone, the size of the cone is determined by an angle that is inputted by the user. The angles used in the simulations were the θ_a reported above. The source led to profiles like the one in Figure 6, where most of the light concentrated in one pixel and then quickly decreased to a lower value.

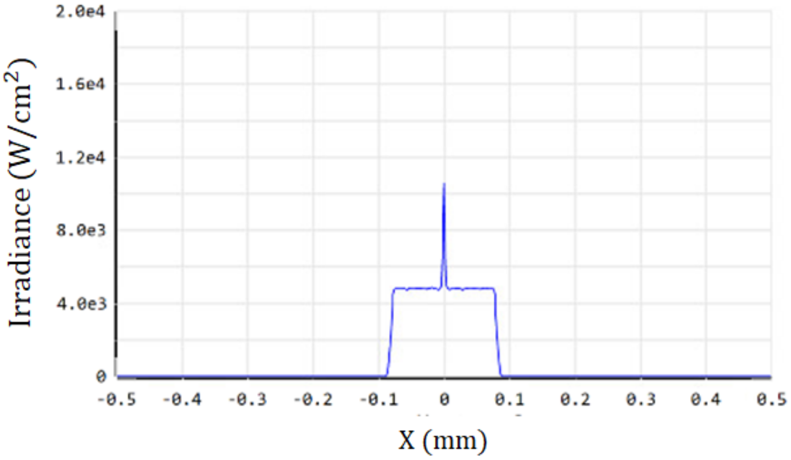

Figure 6: ZEMAX detector at GRIN using point source.

These profiles arose from the fact that the source is finite, and thus some of the rays are emitted at 0 degrees. These rays do not experience total internal refraction (TIR) inside the DCF/SMF core, but go straight through the middle, concentrating in the center of the output beam.

3.4 Gaussian Source

ZEMAX's Gaussian light source has a Gaussian intensity profile. It has two input parameters that determine the beam's width and divergence angle. To avoid the same problem encountered with the point source, it was decided that the SMF/DCF would not be simulated. Instead, the light would be simulated as it is outputted from the SMF/DCF.

The sources were modeled with a $1/e^2$ diameter equal to their respective core diameters: 9 µm for the DCF and 8.2 µm for the SMF (the mode field diameter (MFD) of the fibers should have been used instead). The divergence angle of the source, was determined by a parameter called *position*, which was defined as the distance from the apparent point of divergence of the rays to the source plane location. The position parameters used to imitate the NA of the SMF/DCF were calculated to be 29 µm and 37 µm for the SMF and DCF respectively, using the sketch shown in Figure 7.

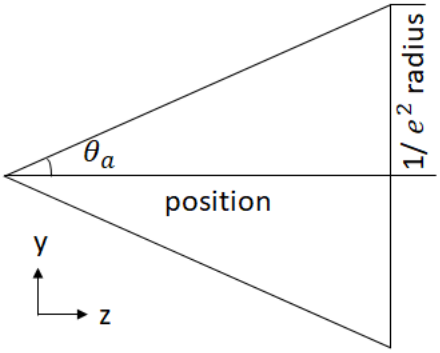

Figure 7: Sketch used to calculate position (divergence of source), using calculated parameters θ_d and $1/e^2$ radius.

3.5 Fiber characterization

3.5.1 Collimator Design

To achieve sufficient resolution, the collimators need to increase the diameter of the beams as much as possible before focusing. This was done by gradually increasing the outer diameter (OD) of the fibers used to build the collimators. To do this, the SMF/DCF are spliced to two multi-mode fibers (MMF) with increasing OD and then glued to a GRIN lens. The MMFs serve as spacers, to allow the beam to diverge, before reaching the GRIN lens. It was necessary to increment the ODs of the fibers gradually in order to be able to splice them together, since their cleaving tensions need to be compatible. For example, the SMF/DCF have a maximum cleaving tension of 600 g, and the MMF with the smaller OD has a minimum cleaving tension of 580 g, thus the tension to cleave the MMF once spliced to the SMF/DCF is limited to the range of 580 to 600 g. If the cleaving tension was higher, the SMF would break and if it was smaller the MMF would not be cleaved properly.

A conceptual drawing of the optical system is shown in Figure 8, and the specifications of the fibers to be used to build the collimators are displayed in Table 1.

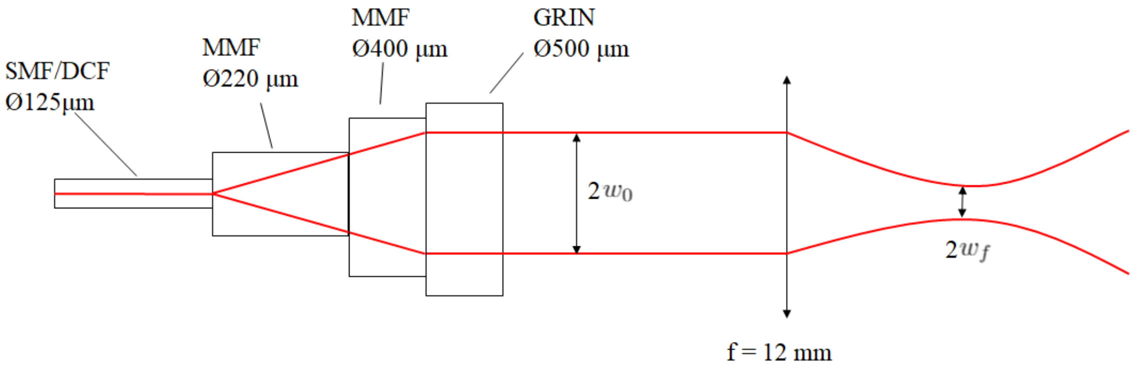

Figure 8: Optical system design, fiber collimator followed by lens and beam (in red) illustration.

Name	Part name and company	OD (µm)	Core diameter (µm)
SMF	SMF-28, Thorlabs Inc., Newton, NJ	125	8.2
DCF	SM-9/105/125-20A Nufern Inc., East Granby, CT	125	9
MMF1	FG200EUA, Thorlabs Inc., Newton, NJ	220	200
MMF2	FP400ERT, Thorlabs Inc., Newton, NJ	425	400
GRIN	GT-LFRL-050-025-50, GRINTECH GmbH, Jena, Germany	500	N/A

Table 1: Collimator fibers specifications

Both of the collimators will support OCT, the DCF will also support NBI, using its core for both OCT and NBI illumination, and the inner cladding for detection of the NBI backscattered signal [68]. The OCT images will be used to perform the DMDI algorithm, and correct both the NBI and OCT images.

3.5.2 Fiber Simulation

In order to simulate the behaviour of the optical system in ZEMAX, it was necessary to simulate the fibers that will be used to build the collimators.

SMF and DCF

As stated in the previous section, these fibers were omitted since it was decided that the light path would begin at MMF1.

MMFs

The MMFs are step-index fibers, in which the inner cladding has a higher index of refraction than the outer cladding. The inner cladding was simulated with silica, as stated by the specification sheets of the manufacturers, and the outer cladding was simulated with F-doped silica since it has a lower index of refraction.

GRIN

The GRIN profile was downloaded from the GRINTECH downloads page, and adapted to be used in ZEMAX's non-sequential mode.

3.5.3 Collimator Realization

There was not enough time for the realization of the collimators; since the GRIN lenses needed to be custom-made by GRINTECH they would take several weeks to be made and shipped. Thus the fibers were not fabricated, however the process of fabrication was determined to be as follows:

1. Splice SMF/DCF to MMF1
2. Cleave MMF1 to required length
3. Splice MMF2 to a NCF with OD 200 μm
4. Cleave MMF2 to required length to meet requirements
5. Splice SMF/DCF-MMF1 to MMF2-NCF
6. Polish NCF off
7. Adhere GRIN lens to MMF2 with UV-curing adhesive

The order of steps was determined by the minimum and maximum cleaving tensions of each fiber. The NCF in step 3 was needed to be able to properly cleave MMF2 to the desired length. If it was to be spliced directly onto MMF1, the splice between the SMF/DCF and MMF1 would break off when the MMF2 was cleaved.

For steps 6 and 7, there would be a need to make tools that would allow for the polishing of the NCF at 0 degrees, and for the alignment of the GRIN lens with the rest of the collimator.

3.6 Beam collimation optimization

3.6.1 Background

It is essential to ensure that the GRIN lens has the required working distance to collimate beams emitted by spacers of different lengths. Thus, the length of the GRIN needs to be changed as the total MMF length changes. This section will outline how the lengths of the MMF1, MMF2 and GRIN are determined and how they depend on each other.

3.6.2 Methodology

The function of MMF1 and MMF2 is to expand the beam as much as possible without modifying the beam's Gaussian shape. Given that the SMF and DCF have different NA and core diameters, the simulations for each were done separately.

The maximum MMF1 lengths for the SMF and DCF were determined by varying its length over a range of values and measuring the profile of the emitted beam at its output face. The maximum MMF1 lengths selected were the ones in which a maximum of 0.1 % of power was lost.

The length of the GRIN was determined using a merit function. MMF1 was set to its maximum value, the length of MMF2 was used as the independent variable, and the length of the GRIN as the dependent variable. The property that was optimized was the collimation of the beam. There is not a direct way to measure whether or not a beam is collimated in ZEMAX, so the merit function was set up with three detectors and used the function 'EQUA'. The detectors were placed 7 mm apart from each other, as seen in Figure 9. The function 'EQUA' is defined in the ZEMAX's documentation as a function that ensures two items are equal within a tolerance set by the user. For this merit function, the items being equalized were the beams' RMS spot size at the three detectors.

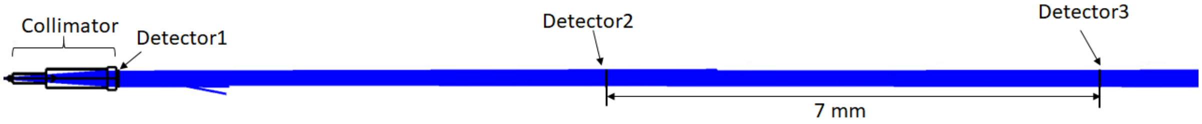

Figure 9: Experiment Set-up for collimation of beam

The experiment was run by setting MMF2 to lengths in the range of 175 µm to 975 µm for the DCF, and 75 µm to 775 µm for the SMF, and then running the merit function. The merit function was used to find the ideal GRIN length that would collimate the output beam of said MMF total length.

3.6.3 Results

The maximum MMF1 length for the SMF and DCF were determined to be 625 µm and 750 µm respectively, and the output beam of both fibers had a spot size of approximately 126 µm. If MMF1 was simulated with a longer length, the power loss due to MMF1 would be higher than 0.1 %.

MMF1 and MMF2 have the same index of refraction and serve the same purpose. Thus, the total length of the two fibers determines the width of the beam at the output of MMF2. More specifically, the length of MMF1 and MMF2 depend on each other, if MMF1 is made shorter, MMF2 should be longer and vice versa.

The relationship between the total MMF length and GRIN for both the SMF and DCF can be seen in Figure 10. It was found that the MMF length and GRIN length have an inverse relationship, thus as the spacer length increases the required GRIN length decreases.

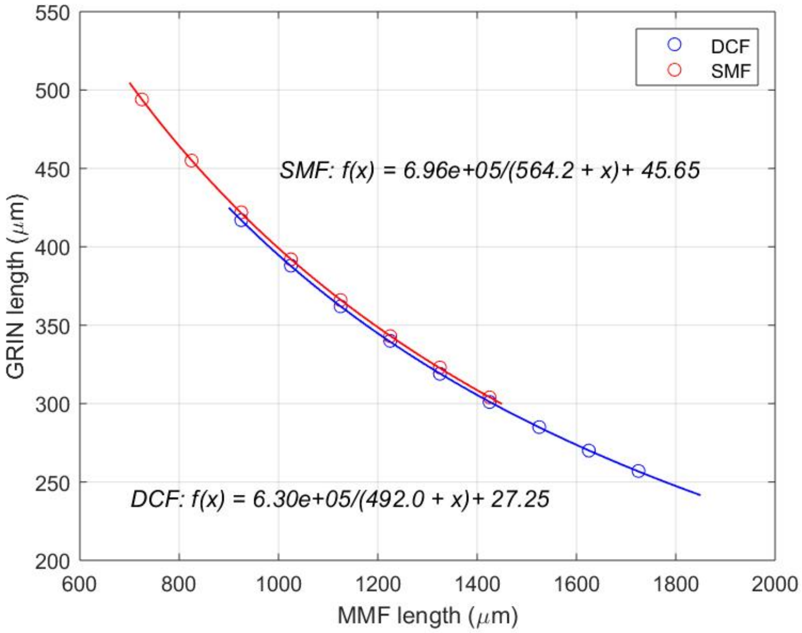

Figure 10: GRIN length vs MMF2 length to collimate beam.

The data obtained was fitted using MATLAB's curve fitting application *cftool* using an inverse function with the shape of $f(x) = \frac{a}{b+x} + c$. The fitted lines will allow for the determination of the ideal length of the GRIN once spacers have been cleaved and measured.

3.7 Resolution

3.7.1 Background

The resolution of the system is of utmost importance because it will determine which tissue properties will be resolvable in the scans. As per the requirements, the GEI needs to be able to resolve gastric pits, which have a size of 50 to 70 µm [10].

The resolution of the GEI has been defined as the FWHM of the beams, where the FWHM is the diameter at which the intensity of the beam is half of its highest value. In order for a feature to be resolved, it should have a minimum size of the system's FWHM. If the feature is any smaller it would not be resolved.

3.7.2 Methodology

The FWHM was calculated for each MMF-GRIN combination using the following formula:

$$2\omega_0 = \frac{4f\lambda}{\pi D(2\sqrt{\ln 2})} \tag{2}$$

where ω_0 is the half width half max of the beam at the focal plane, f is the focal length of the scan lens (12 mm), λ is the wavelength of the light source, and D is the $1/e^2$ spot size of the beam emitted from the GRIN lens. D was measured with a detector located at the output face of the GRIN (Detector 1 in Figure 9). The factor of $2\sqrt{\ln 2}$ allows for the calculation of the FWHM instead of the $1/e^2$ spot size.

The calculations were done using the central wavelength of the OCT's light source, 1310 nm. The FWHM is proportional to the wavelength, thus if it is ensured that gastric pits are resolvable by the OCT system, they will also be resolvable by the NBI system.

The data points were fitted with inverse functions, as in the previous section.

3.7.3 Results

Figure 11 displays the FWHM of the system at the focal plane against the total MMF's length.

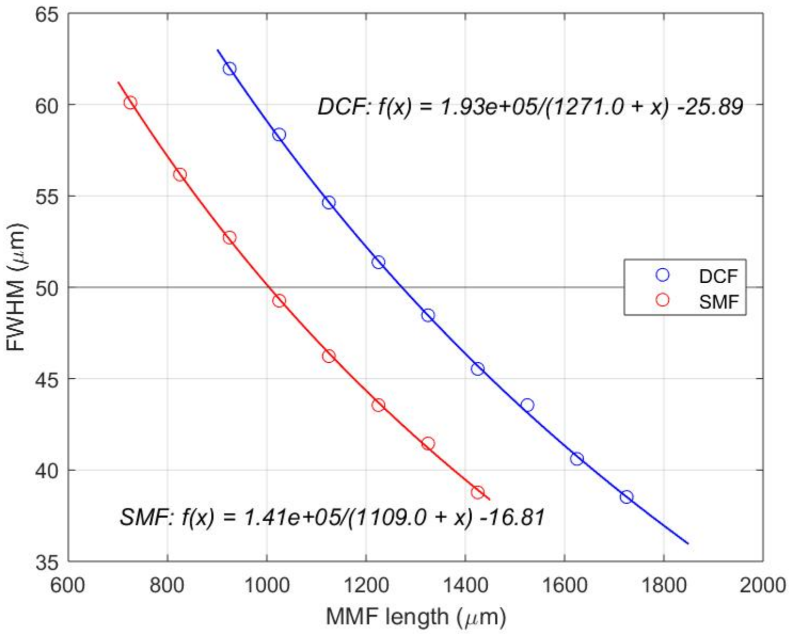

Figure 11: Spot size at focal plane vs MMF length.

In order to meet the resolution requirement the fitted lines were equalized to 50 µm and solved to find the minimum total MMF length required. For the DCF, the minimum MMF length is 1272 µm, and for the SMF it is 1001 µm. Any spacer combination longer than that would meet the resolution requirement. If shorter, the system would not be able to resolve gastric pits.

3.8 Power Loss

3.8.1 Background

Power loss is the amount of optical power that is lost in an optical system, which can be due to factors such as connectors, splices, and fibers. It is used to calculate power budgets of systems to ensure signals are measurable by the detectors [67]. It is calculated using the following formula:

$$P_{loss} = 10 \log_{10} \left(\frac{P_{remaining}}{P_{total}} \right) \tag{3}$$

where P_{loss} is the power loss in dBs, which is calculated as the ratio between the power that was not lost ($P_{remaining}$) and the source's total power (P_{total}).

Using the collimator design described above, there are two design components that can generate power loss. Firstly, the splices and the interface between MMF2 and the GRIN lens. These power losses are unavoidable, but can be reduced by ensuring proper splicing and positioning. Secondly, there is power loss from the rays that reflect off the MMFs' cladding. As the length total length of the MMF increases, a larger amount of light overfills the GRIN lens and is lost or scattered in an undesirable manner. Thus, it increases the amount of power loss. These rays are not collimated, and can also add noise if they scatter back into the probe.

3.8.2 Methodology

The system's power loss was measured in ZEMAX, using an absorbing disc surface and a detector afterwards. MMF1 was kept to a constant length, and MMF2 was varied over the same ranges as described in the previous sections. At each MMF2 position the power loss was measured.

The absorbing disc (radius 250 µm) absorbed all the rays that form part of the collimated beam, then the detector detected the rest of the rays which were not collimated. The two surfaces were not put directly in front of the end of the GRIN, so that the rays reflected from the MMF's cladding had enough space to deflect, as seen in Figure 12.

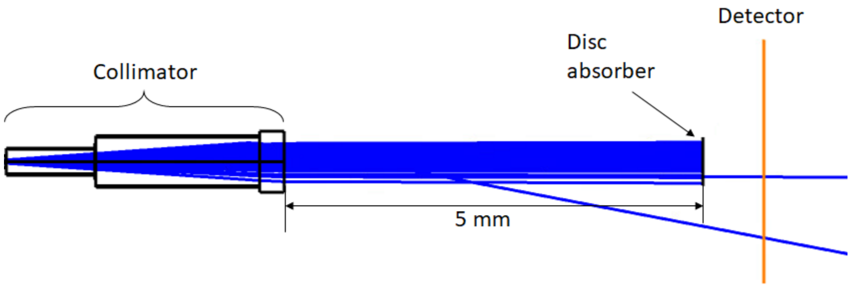

Figure 12: Power Loss experimental set-up

To determine whether a MMF2-GRIN combination had an acceptable amount of power loss, it was compared to the power loss that occurs in a regular splice, which is -0.05 dB or 1.14 % (found using Equation 3). In the simulations conducted 1.14 % is equivalent to 11.4 mW since the total source power used was 1 W .

The simulation results were fitted analogously to the diagram shown in Figure 13, since laser beam propagation can be approximated by assuming a Gaussian intensity profile.

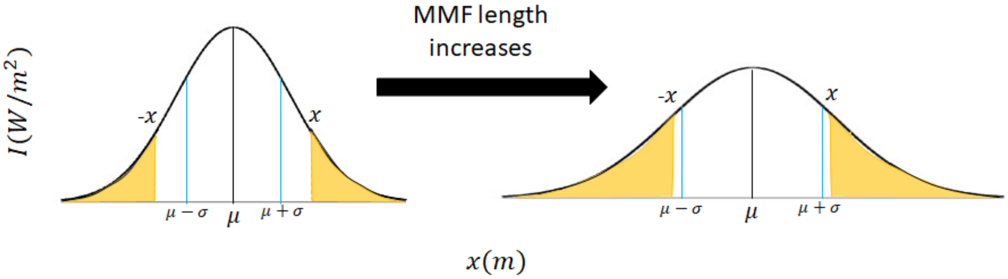

Figure 13: Power loss analysis model. Yellow section is power loss.

As shown in the Figure, as the MMF length increases the Gaussian shape flattens and the highlighted area, the power loss, increases. Thus, power loss was fitted with the following equation:

$$P_{loss} = A_0 + 2A(\text{erfc}(\frac{x-\mu}{\sigma})) \tag{4}$$

where erfc is the complementary error function, σ is $1/e^2$ width of beam at MMF2's exit, which is proportional to the standard deviation of the curve (as seen in Figure 13), A_0 is the fixed power loss due to MMF1, x is the radius of the collimated beam (250 µm), and μ is an horizontal shift that corresponds to the MMF2 length at which the rays begin to reflect from the cladding. The factor of two is due to the definition of the erfc function in excel.

3.8.3 Results

In Figure 14a, the power loss vs. MMF length is shown for the three different wavelengths for both the DCF and SMF. As the MMF length increases, the power loss and resolution increase. Thus a higher resolution leads to more power loss, so in order to determine the best optical design, a compromise must be reached.

Given that the power loss is higher for the 450 nm source, the DCF and SMF 450 nm curves were fitted with Equation 4 and solved for 11.44 mW.

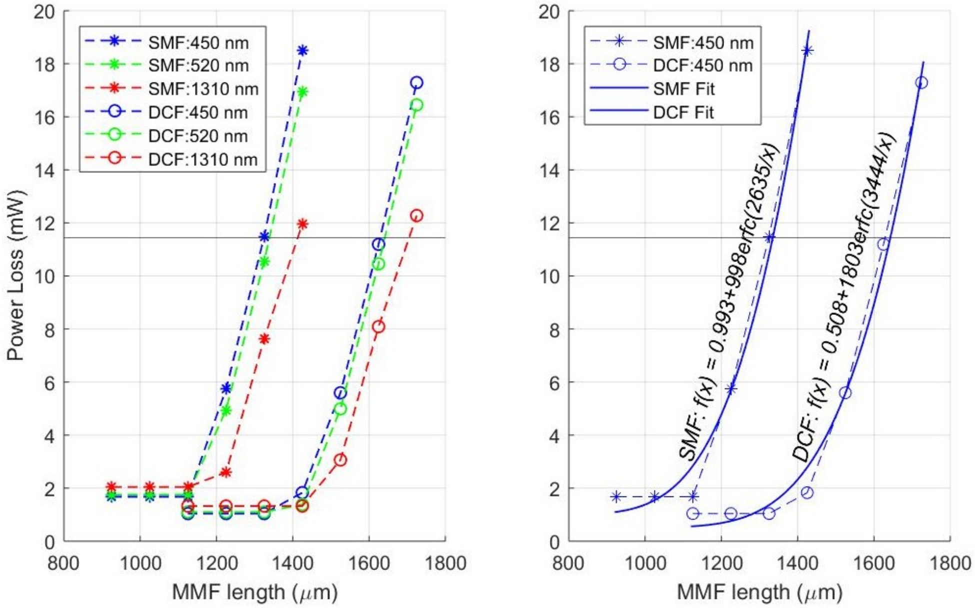

Figure 14: Power loss vs MMF length

The maximum total MMF length for the DCF and SMF collimators were found to be 1643 µm and 1335 µm respectively. Using the equations found in Section 3.7 Figure 11, the maximum resolution achievable with the collimators is 40.9 µm.

3.9 Current State

In this section, simulations were conducted to find the required collimator parameters to meet the set requirements. Equations to describe the relationships between the MMF length and GRIN length, the MMF length and FWHM, and the MMF length and power loss were found.

The MMF total length for the DCF to meet the requirements is in the range of 1272 to 1643 µm, and for the SMF it is in the range of 1001 to 1335 µm. The required GRIN length to collimate the beams with such MMF lengths can be found using the equations in Section 3.6 Figure 10. Using these MMF length ranges, both the SMF and DCF can achieve a FWHM in the range of 40 to 50 µm (for the 1310 nm source), which corresponds to a depth of field of 2 to 3 mm.

3.10 Future work

There are several things that still need to be done for the optical system of the GEI. The focus shift for the specified MMF ranges needs to be simulated, since the beams are not perfectly collimated the spotsize will not be at the focal length of the lens. Additionally, the collimators need to be fabricated to evaluate how accurate the simulations are.

The simulations were only conducted for the on-axis behaviour of the system. The off-axis behaviour of the system still needs to be characterized. The field curvature, best position to ensure a 1:1 scan magnification, and spherical and chromatic aberrations need to be simulated. To do this, it is necessary to test several lenses or lens systems and determine which ones would minimize aberrations.

4 Mechanical System

4.1 Overview

This chapter describes the design and testing of the mechanical sub-system of the GEI, the function of which is to physically manipulate the fibers for large FOV scanning. The system uses inexpensive, commercially available coin DC motors that are frequently used as vibrators for electronic devices like cell phones and haptic displays. The motor's rotor is fitted with a custom attachment that translates the rotational motion of the motor into linear scanning motion of the optical system.

The main research achievements described in this chapter are:

1. Design of the **rotor attachment**, which converts the motor's rotational motion into linear scan motion.
2. Design of the **housing**, where the mechanical and optical systems interact.
3. Measurement of **scan amplitude** and its dependence on experimental variables.
4. Quantification of **scan stability** and how it is affected by experimental variables.
5. Measurement and dependence on operating voltage of the fibers' **scan frequency**.
6. Determination of the GEI scanner **lifetime**, which is the time during which the scanner works consistently.

Finally, a summary of the current state of the GEI prototype and its characteristics will be presented for future implementations of the device. It includes the size, scan amplitude and frequency, that can be achieved with the current state of the GEI.

4.2 Requirements

The mechanical system of the GEI has been designed to meet the following requirements:

1. **Scan Amplitude**
   The GEI will be attached to an Olympus EVIS EXERA II (Olympus America Inc., Cypress, CA), which is the most common scope used in the Vancouver general hospital (VGH) Gastrointestinal (GI) endoscopy clinic and has an OD of 9.9 mm. For the GEI to have a large FOV and perform DMDI, the fibers need to have a large scan amplitude, which was determined to be 9 mm to approximately match the OD of the endoscope. A 9 mm scan amplitude, along with DMDI, leads to a larger FOV than other forward-viewing point-scanning mechanisms, which have been reported to have a scan amplitude of 3 mm by 3 mm [62, 63, 65].

2. **Scan Frequency**
   To optimally match the scan resolution to the A-line (OCT) and pixel (NBI) sampling resolution, Equations 5 and 6 were used to calculate the required scan frequency of the GEI's fast axis. This ensures the scans acquired by the GEI are not undersampled. To perform this calculation, it was assumed that the scan pattern of the fibers was a triangle wave with a period T_{scan}:

$$n_{sample} = \frac{scan\,amplitude}{2w_0} \tag{5}$$

$$f_{scan} = \frac{1}{T_{scan}}, \qquad T_{scan} = \frac{1}{f_{laser}}(2n_{sample}) \tag{6}$$

   where n_{sample} is the number of resolvable spot sizes in a scan, which is equal to 180 when using a scan amplitude of 9 mm and a spot size ($2\omega_0$) of 50 µm. In Equation 6, f_{laser} refers to the A-line acquisition frequency of the OCT's laser, 100 kHz, which makes the GEI fast axis scan frequency 277 Hz.

   Assuming the gastroscope's distal end has a constant speed, and given the target scan amplitude and frequency, a slow-axis scanning speed of 2.7 cm/s for full resolution imaging has been calculated, which allows for an area scan speed of 2.43 cm^2/s.

3. **Stability**
   The GEI should scan in a stable manner, so that DMDI can be performed. If the scan pattern is not stable, the images cannot be properly co-registered and corrected.

4. **Size**
   The last requirement of the GEI is to minimize its overall size. The GEI is designed to be attached to the distal end of a gastroscope and needs to be comfortable for the patient, thus the GEI should be as small as possible. The maximum size of the GEI was determined based on the size of variceal banding ligator, a gastroscope-deployed device which also attaches to the distal end of gastroscopes and increases the OD of the tip [69]. Our goal is to increase the total area of the gastroscope's distal end by no more than 20% of the size of the ligators.

The following coordinate system for the GEI is defined: the two fibers are scanned parallel in the y-dimension (fast-axis), are maintained at a fixed separation in the x-dimension (slow axis), and by the right-hand rule the z-direction is along the tissue's depth (Figure 15).

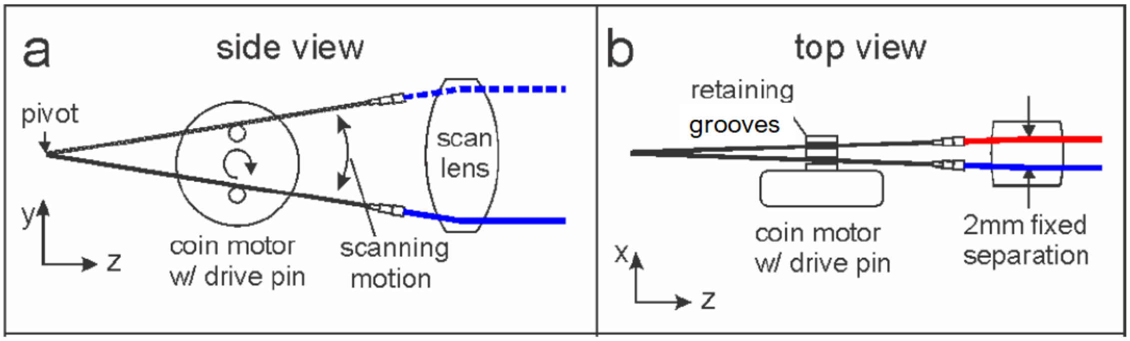

Figure 15: Mechanical system conceptual design, a) side view and b) top view. Blue and red lines are the light beams emitted from the collimators. The labeled retaining grooves and pin are part of the rotor attachment.

4.3 Experimental Set-up

In this section an overview of the experimental set-up used to conduct the experiments regarding the research aims outlined above will be described. A picture of the experimental set-up is shown in Figure 16. The variables and components outlined below will be described in detail in the following sections.

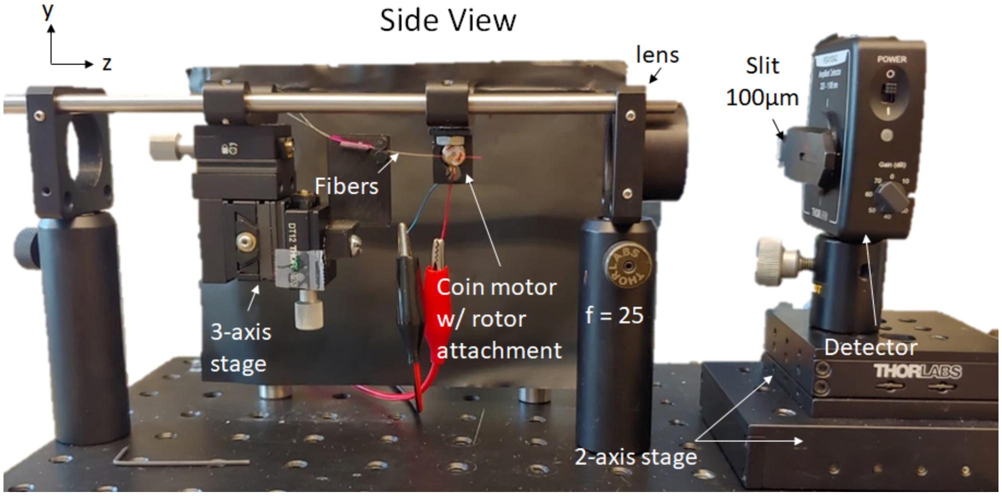

Figure 16: Side view of the experimental set-up for frequency experiment. Detector was switched to a camera for the stability experiments.

The detectors used in the experiments, a photodetector and a camera, were put on optical posts to allow for adjustment in the y-direction; in the x and z directions a 2-axis stage was used to center the GEI's scans on the detectors and to ensure the detectors were in the focal plane of the lens. The light source used to conduct the experiments was a 630 nm laser. A visible wavelength was used rather than an infrared one because it led to a more efficient and faster experiment set up, which was necessary to center the scans on the detectors.

As stated in the previous chapter the optical system was not fully realized, so the majority of the experiments were done with cleaved 125 μm SMFs. One downside of not having the fibers made is that light diverges quickly once it leaves the SMFs. Additionally, the oscillation of fibers will not behave in the same way as they would with the collimators attached. In order to collect as much of the SMFs' light as possible, the shortest focal length lens available in the lab was used ($f = 25$ mm).

In order to describe the experiments, it is necessary to define the following variables: the total length of the fiber from the pivot point to the tip (l_{fiber}), the fiber length from the pivot point to the motor (l_{p-m}), the fiber length from the motor to the tip of the fiber (l_{m-t}), and preload, which is the downward force the fibers make on the rod. Preload is varied by changing the pivot's y-position (y_{p-m}) and the angle of the fiber platform (θ_{fiber}). When a set-up has zero preload it means that at the lowest motor position the fibers are not exerting any force on the grooves of the rotor attachment. Lastly, the y-span quantifies the eccentricity of the rotor attachment, and it is equal to double the distance between the motor axle and the center of the rotor attachment. These variables are all shown in Figure 17.

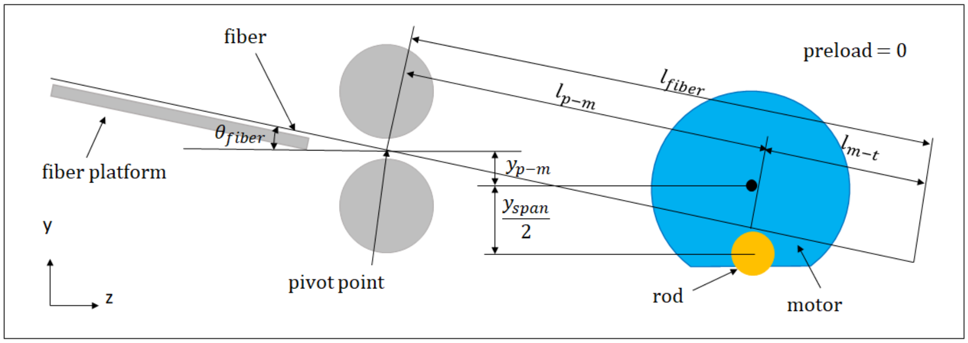

Figure 17: System sketch with variables definition

4.4 Rotor Attachment

4.4.1 Background: Motor

The motor used for the experiments was a vibrational coin DC brush motor (C1030B028F, Jinlong Machinery & Electronic Co. Ltd., China), shown in Figure 18. The motor has a total thickness of 3 mm and has two different components: its stator (OD 8 mm), and rotor (OD 7.5 mm).

The rotor, as seen in Figure 18c, is asymmetrical: the rounded side has an extra weight and the cut-off side is lighter, leading to an unbalanced rotor and making the motor vibrate. For the purposes of the GEI, a motor that vibrates is not desired because vibrations lead to unstable scan patterns, making the DMDI algorithm impossible to perform. Thus, some design considerations, which are outlined below, were taken in order to minimize vibrations. Vibrational motors were used because they are inexpensive, which would make the GEI more affordable. Additionally, the rotor attachment can be designed to aid balance the motor.

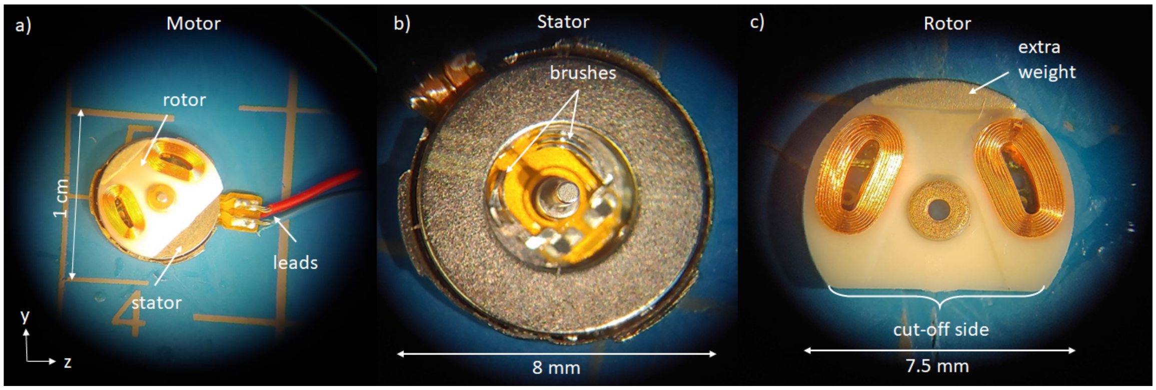

Figure 18: Motor images a) whole with outer casing removed b) stator and c) rotor.

This specific motor was chosen because its OD is smaller than the gastroscope's OD, thus it will not increase the gastroscope's size in the y-direction. It is rated at a higher rpm than the majority of other DC coin motors. Smaller motors were not used because it was found that, as described later, it is advantageous to have larger rotors to achieve larger scan amplitudes.

4.4.2 Design Considerations

The rotor attachment is affixed to the motor rotor with adhesive. It converts the rotational motion of the motor into the linear scan motion of the fibers. It has a rod on which the fibers rest, which is used to actuate the scanning pattern.

One of the design considerations for the rotor attachment was the position of the rod where the fibers rest with respect to the center: its eccentricity. The eccentricity of the rotor attachment is significant for two reasons: rotor balancing and scan amplitude. The rotor attachment should be placed so that its weight rests on the rotor's light side to balance the rotor and minimize vibrations. The required rotor attachment eccentricity will depend on its mass. Additionally, the eccentricity of the rotor attachment is a key parameter in determining the scan amplitude. Finally, the rotor attachment needs to have grooves to maintain 2 mm separation between the fibers (Figure 15).

4.4.3 Printed rotor Attachments

The first iterations of the rotor attachment were 3D printed, using a stereolithography printer (PICO2, ASIGA, Sidney, Australia) with a transparent resin. The two designs had a base that was designed to be glued onto the rotor.

The rotor attachment shown in Figure 19 was a practice one. It aided in the learning of SOLIDWORKS, 3D printing, and an understanding of the small dimensions that were dealt with during this project. The practice rotor attachment had a base with a thickness of 2 mm and a rod with a height of 3 mm, which in retrospect were unnecessarily thick (Figure 19). Furthermore, the rod was not able to maintain the position of the fibers due to the lack of grooves, allowing them to immediately fall off the rod as the motor started rotating.

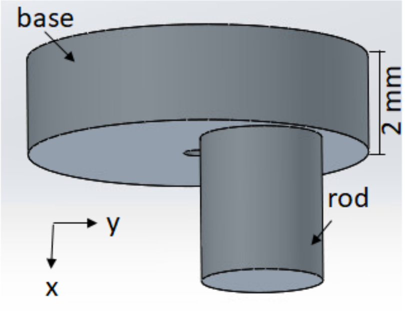

Figure 19: First rotor attachment design.

The second printed rotor attachment, shown in Figure 20, featured the addition of a groove on the rod and the base was thinned to 1 mm. The design shown in Figure 20 only has one retaining groove because the housing being used at the moment was not equipped to position two fibers. Had the groove functioned satisfactorily, the design would have been modified to have two grooves. The position of the rod and the addition of the groove, gave the rod a y-span of 7 mm, which allowed for the easy completion of the scan amplitude requirement.

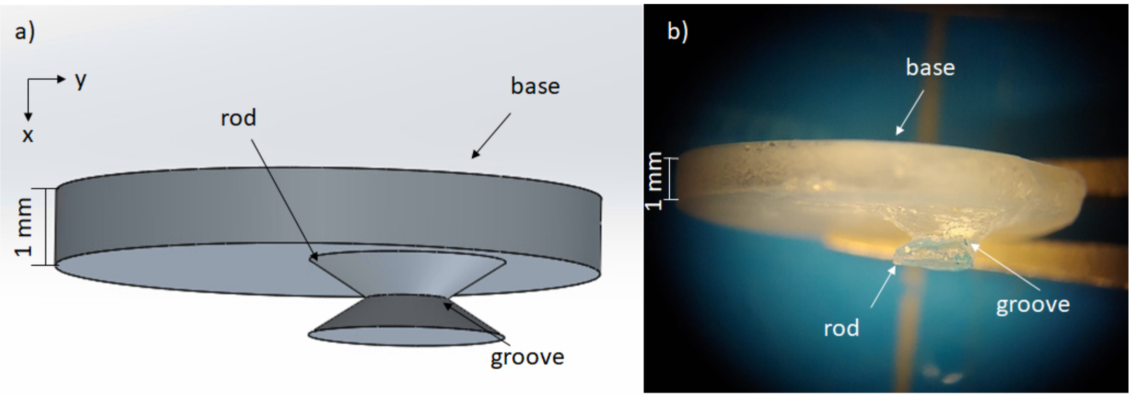

Figure 20: Second rotor attachment design, a) SOLIDWORKS design, b) 3D printed and polished result.

Upon fabrication, it was observed that this rotor attachment was difficult to 3D print. It was printed in the positive x-direction, but the groove was not fully supported as it printed, and thus did not print accurately (as seen in Figure 20b). Consequently, the fibers jumped out of the uneven groove during rotation.

4.4.4 Machined rotor attachment

After several attempts at printing the rotor attachment, it was decided to machine rods using small diameter brass rods (1.83 mm OD). The grooves were made 2 mm apart on a lathe. The grooves on these rods were deeper and sharper than the ones 3D printed. It was desired that the grooves were made even sharper and more v-shaped instead of u-shaped as seen in Figure 21, so the fibers would have been more constrained inside the grooves.

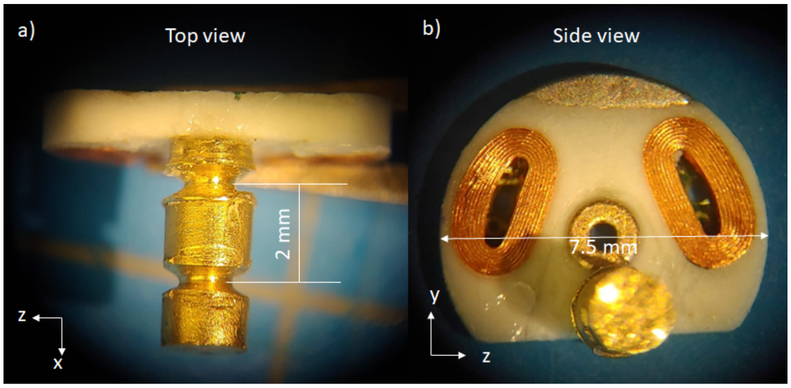

Figure 21: Machined rotor attachment a) top view, and b) side view, glued using jig.

The rods were directly glued onto the rotor's cut-off side (Figure 21), in an attempt to stabilize the motor and reduce vibrations. The rod used for the experiments described below was glued 1.85 mm away from the center, and had grooves that were 0.3 mm deep, which gave the rod a y-span of approximately 3.7 mm.

In order to glue the machined rods onto the rotor and ensure that they were orthogonal to each other, a jig (Figure 22) was designed and printed. The rotor is placed on the rotor seat and the jig is flipped upside down. Then epoxy is applied to it, the rod is put inside the slit and pushed onto the rotor.

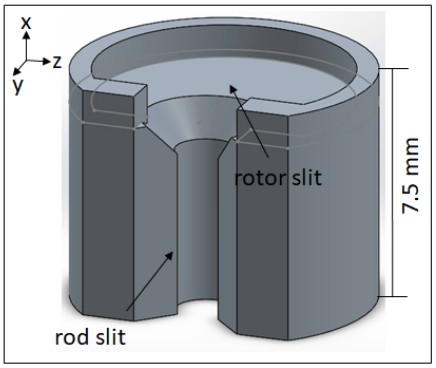

Figure 22: Jig for machined rotor attachments, used 180 degrees rotated in the y-direction but shown this way to ease visibility.

4.5 Housing

The housing encloses the environment in which the optical and mechanical systems interact. The major components of the housing were 3D printed using the filament printer Ultimaker 2+ (Ultimaker, Netherlands).

4.5.1 Design Considerations

Firstly, the housing should align with the scan lens ($f = 25$ mm), so that the light can be collected and focused onto the detectors. Secondly, the motor and fibers need to be able to move freely in the z-direction because this allows for the positioning of the fibers with respect to the scan lens. Thirdly, the housing should ensure that the fibers scan at 2 mm apart from each other in the x-dimension.

4.5.2 Previous Versions

There were three iterations of the housing that were fabricated before arriving at an acceptable testing prototype, which was used to analyze the mechanical system of the GEI in the following sections.

The first two iterations, shown in Figure 23, did not have any degrees of freedom because they were designed to be attached directly to an optical breadboard. Thus, no components of the housing could move freely in any direction. The housings did not have a place onto which the fibers could be placed, therefore the fibers had to be positioned using tape, which made the positioning of the fibers imprecise and hard to recreate.

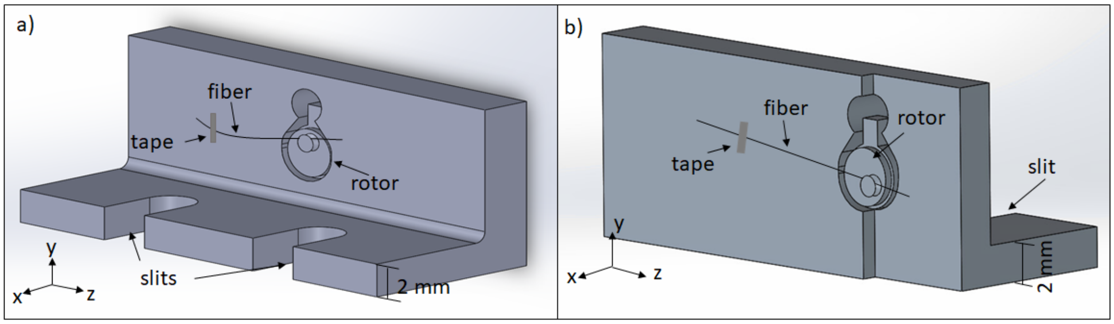

Figure 23: GEI benchtop housing a) first and b) second iterations (second slit not visible). Slits designed to attach to optical breadboard. Fiber attached to housing using double sided tape.

For the third iteration, the housing was modified so it worked with a Thorlabs 30 mm optical cage system, as shown in Figure 24. This modification gave the housing one degree of freedom, in the z-direction, with respect to the scan lens. However, the two fibers could not be placed, and had again to be positioned with tape.

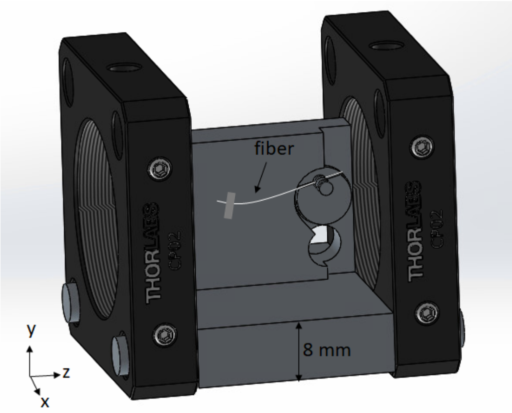

Figure 24: Housing third iteration, compatible with optical cage.

4.5.3 Final testing prototype

From the previous versions, it was decided to keep the housing on the optical cage for two reasons. First, it allowed for easy alignment with the scan lens, since the lens was put on a post to which the cage was attached. Second, it allowed the housing to be moved in the z-direction, so that, the fibers could be moved with respect to the lens and achieve different scan magnifications. This is to ensure that complete scan patterns were captured by the detectors.

Furthermore, from the previous versions, it was noticed that the fibers' pivot position in both the x and y directions with respect to the motor was important for the acquisitions of stable scans. Thus, the acceptable testing prototype of the housing was designed so that the pivot point and motor were able to move with respect to each other. In order to have these capabilities, the housing was split into two parts: the fiber holder and the motor holder. The fiber holder is where the fibers are placed and where the pivot point is located, and the motor holder is where the motor resides. Figure 25, shows all the components of the housing and how they are positioned with respect to each other.

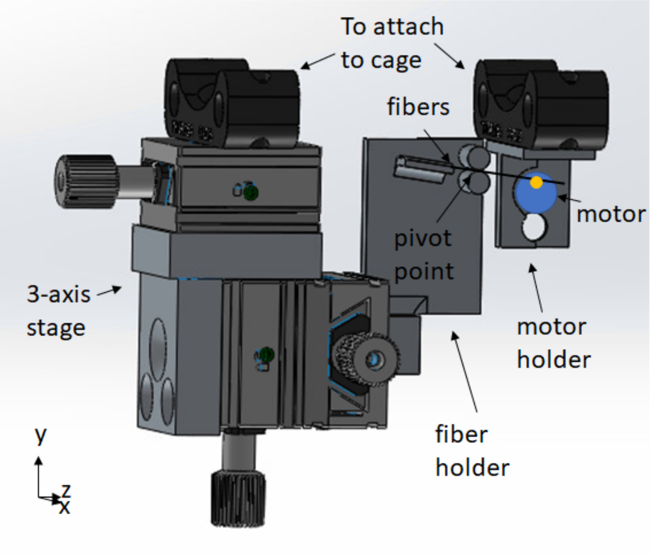

Figure 25: Acceptable testing prototype, compatible with optical cage.

Fiber holder

The fiber holder served the following functions: ensuring the fibers are held 2 mm apart, controlling the position of the fibers' pivot point, and aligning the fibers with the retaining grooves on the rotor attachment. The acceptable testing prototype of the fiber holder is shown below in Figure 26.

The fibers were placed 2 mm apart using a platform with retaining grooves, as seen in Figure 26. The grooves were printed as an insert using the higher resolution resin printer in order to achieve higher design fidelity.

The rods, labeled as pivot rods, were designed so that the position of the fibers' pivot point could be controlled and easily determined. Furthermore, the rods avoided the force due to bending from concentrating on a single spot on the fibers as they scanned. The rods provided a larger bending radius so that the force was distributed along the fibers.

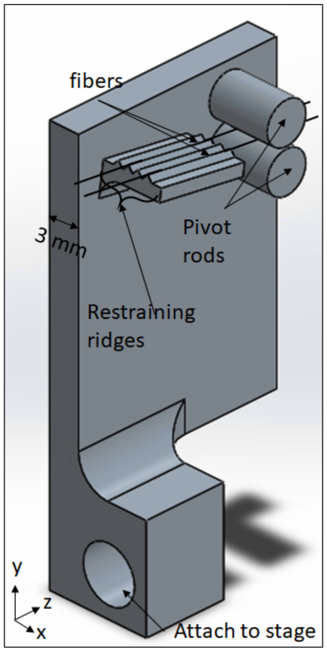

Figure 26: Final housing version: Fiber Holder

In order to be able to move the pivot point with respect to the motor, the fiber holder was attached to a 3-axis translational stage, (DT12/M, Thorlabs Inc., Newton, NJ), as seen in Figure 25. The stage allowed for fine alignment of the fibers with the retaining grooves of the rotor attachment. Additionally, it allows for the movement of the y-position of the pivot point, effectively changing the preload.

To use the stage and fiber holder along with the optical cage, the stage was attached to a cage mounting bracket (CP02, Thorlabs Inc., Newton, NJ), which allowed for coarse movement of the pivot point in the z-direction (as seen in Figure 25).

Motor Holder

The motor holder design was simpler than the fiber holder one, as it was designed and printed to ensure alignment with respect to the scan lens in the x-direction and y-direction. The motor holder used the same cage mounting bracket as the fiber holder. However, given the design of the cage mounting bracket, the only way to attach the motor holder to it was using a nut that would lay in front of the motor, which restricted the view when acquiring data for evaluating the scan amplitude of the fibers (as seen in Figure 27).

4.6 Scan Amplitude

4.6.1 Background

The scan amplitude refers to the distance that the fibers scan along the y-axis. As per the requirement specified above, the scan amplitude should be 9 mm. It is of utmost importance to achieve an amplitude of 9 mm because a large FOV is what differentiates the GEI from other forward point-scanning mechanisms.

The main variables that affect the amplitude are l_{fiber}, l_{p-m}, and l_{m-t}. Thus, an experiment was designed to test the effects of these three variables on scan amplitude.

4.6.2 Methodology

The amplitude of the system was measured through images of the fibers' end in the y-z plane, as seen in Figure 27. The images were taken using a phone with a resolution of 1440 by 3120 pixels. In order to process the images, the motor holder width was measured in pixels and the value was used to compute a pixel to mm converting factor. This ratio was then used to measure the scan amplitude, l_{p-m} and l_{fiber}.

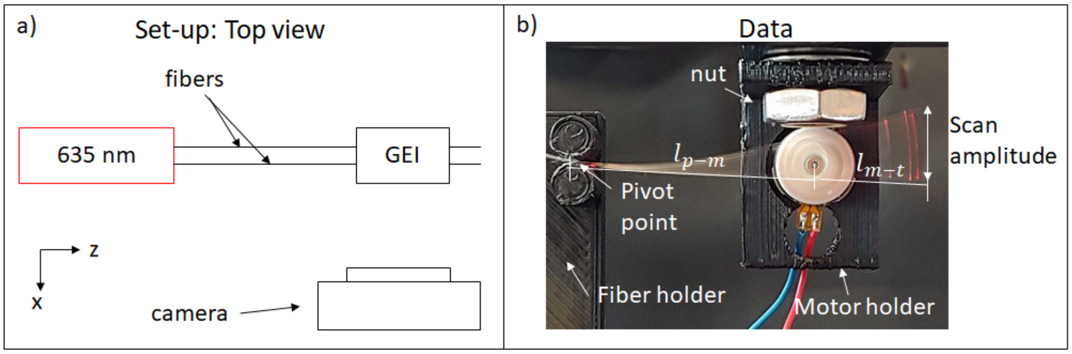

Figure 27: Scan amplitude: a) measurement diagram and b) sample data.

To explore the effects of different l_{fiber} and l_{p-m} on scan amplitude, data was acquired by setting the fibers to a fixed length, moving the motor through four different l_{p-m}, and acquiring images. This process was repeated at nine different l_{fiber} lengths. The known positions were set using a caliper, which allowed for consistency when setting the l_{p-m} at the nine different l_{fiber} and reduce the processing time of the images.

4.6.3 Results

Figure 28 displays the results of the experiment described above. Points labeled with an ‘x’ were not used for curve fitting because the tips of the fibers were not visible due to the nut shown in Figure 27. It can be seen that l_{fiber} and the scan amplitude have a positive linear relationship.

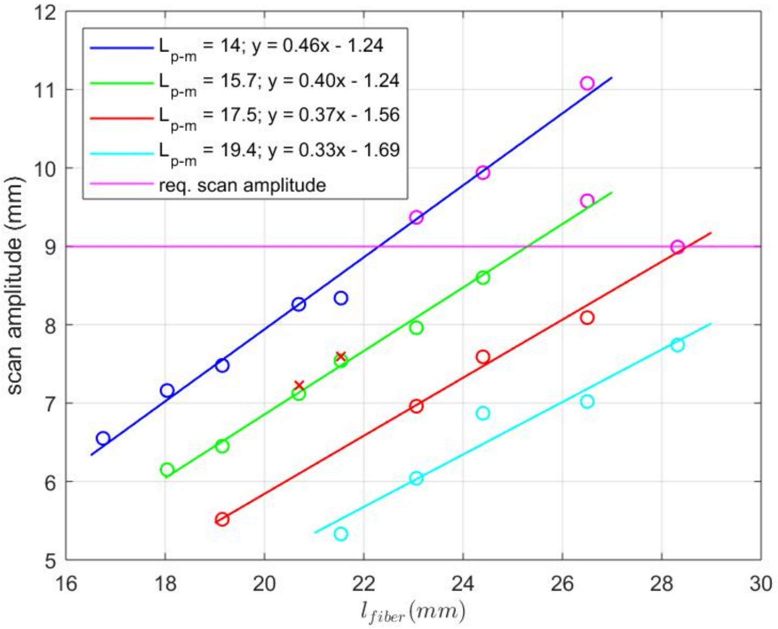

Figure 28: Fiber length vs scan amplitude at different l_{p-m}. Points above the required scan amplitude line (pink) meet the requirement; anything below does not. Points labeled with x were not used for curve fitting.

The figure shows that as l_{p-m} increases, the l_{fiber} required to achieve the scan amplitude requirement of 9 mm also increases. This is the desired behaviour since a smaller GEI is required as per the size requirement. The required scan amplitude (in pink) divides the graph into points that meet the scan amplitude requirements and points that do not, thus points in pink have the desired scan amplitude or higher. A linear relationship between the l_{p-m} and the minimum l_{fiber} needed to achieve a scan amplitude of 9 mm was found, and is shown in Figure 29. The data points were found by setting each of the fitted lines equal to 9 mm and solving them.

As l_{p-m} increases, the l_{fiber} required for a scan amplitude of 9 mm increases by 1.79. This relationship can be used to easily determine what fiber length is required at any l_{p-m}. As per this result, it is best to have the pivot point and motor as close to each

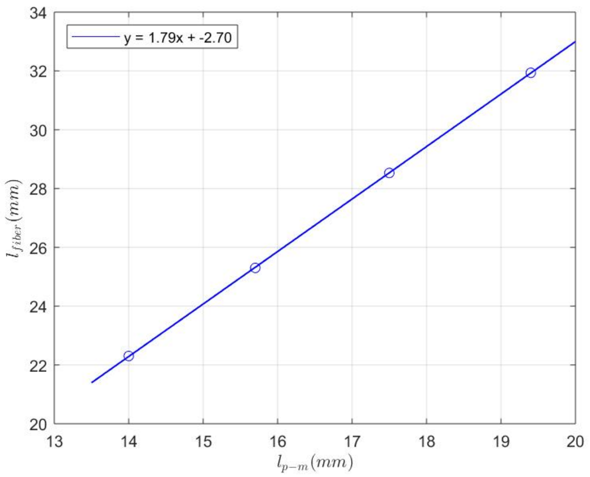

Figure 29: Minimum l_{fiber} to meet requirement vs l_{p-m}.

other as possible.

4.7 Scan stability

4.7.1 Background

The stability of the system refers to how stable a scan is over time, in other words how much the scan pattern changes per frame. It is necessary that the scan patterns are consistent in order to perform DMDI, otherwise the algorithm is not able to properly correct the images of distortion.

There are several factors that affect the stability of the scan, including l_{fiber}, preload, and x-axis alignment. For this project, the effects of fiber length and preload on stability were evaluated. The former was important to understand because the fiber length has a linear relationship with the scan amplitude and thus determines whether the scan amplitude requirement can be met. The latter experiment quantified the effects of preload on the scans. Preload is necessary to minimize the effects of gravity on the cantilevered fibers, allowing the GEI to work in different orientations, such as upside down or sideways.

4.7.2 Methodology

The stability of the system was measured using a camera (winCAM D-LCM, DataRay Inc., Redding, CA), which was positioned at the image plane of the lens. A diagram of the experimental set up in shown in Figure 30.

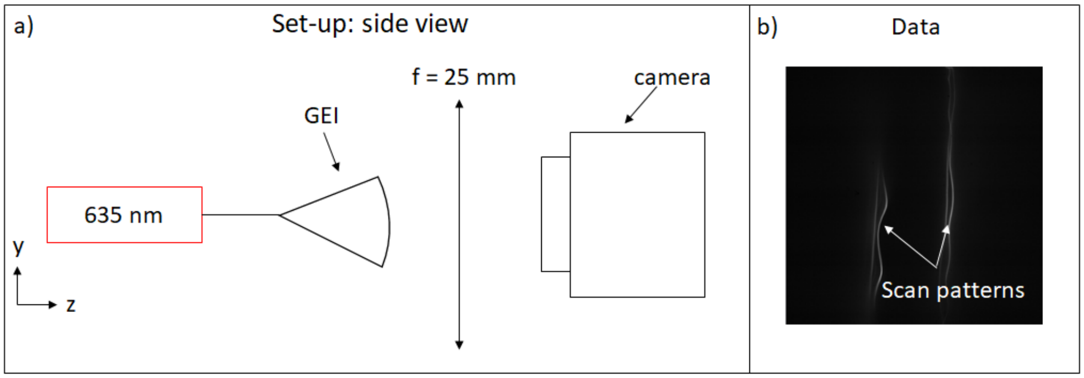

Figure 30: Stability experimental set-up, a) diagram and b) sample scan patterns acquired by camera, using two fibers.

In order to determine the stability of a scan, five consecutive frames were taken in the x-y plane and compared. The MATLAB function *corr2.m* was used to calculate a correlation coefficient (r) between two consecutive frames. Then the average of all the correlation coefficients was taken, defined as $\overline{r}$, which has a range from 0 to 1. If $\overline{r}$ is close to 0, the frames are not similar thus the system is unstable; if $\overline{r}$ is close to 1 the frames are similar, which means the system is more stable. Figure 31 shows a comparison of what a stable scan vs an unstable scan look like.

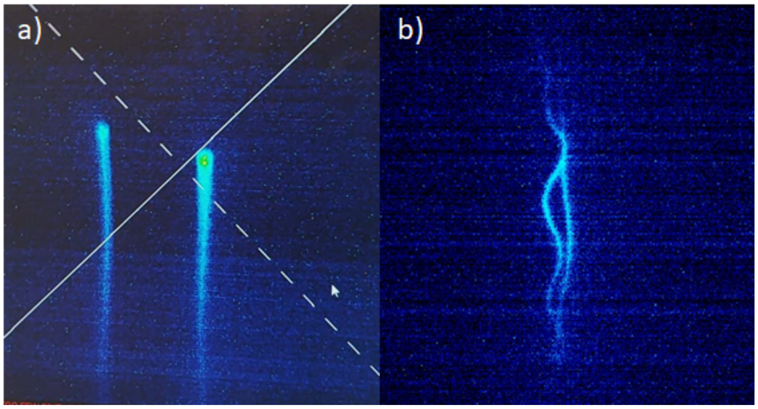

Figure 31: Stable vs unstable scan comparison a) stable taken with two fibers, b) unstable taken with one fiber. These images were acquired with screenshots of the camera's program.

The images were pre-processed by normalizing them (0-1 range) because the intensity across image sets varied significantly. This is due to the fact that the exposure time of the camera was not constant over all set-ups. If the experiment was to be repeated the exposure time would be set to a constant value over all the frames to avoid large intensity variations. Other pre-processing methods were tried such as binarization in combination with different morphological operations (open, close and erosion of images). However, these operations led to correlations that were not accurate to what was perceived. The standard deviation of the correlation coefficients between all images were calculated, to infer in the precision of $\overline{r}$.

As stated above there were two experiments conducted: stability vs. fiber length and stability vs. preload. The former was performed by changing the fiber ratio, which is the ratio of l_{p-m} over l_{m-t}. The fiber ratio was varied by changing the position of the motor holder with respect to the fiber holder. The experiment was performed at two different l_{fiber} lengths (24 mm and 32 mm), to see whether the total length of the fiber had an effect on the stability of the scans. The preload was kept constant during this experiment. The scan amplitude was measured at every fiber ratio, to analyze stability vs. scan amplitude.

The second experiment was conducted by changing the preload of the system and recording images for stability analysis. The preload was varied by changing y_{p-m}, using the 3-axis stage in Figure 25. It is reported as the absolute of the difference between the new y_{p-m} position and the y_{p-m} at the zero preload position (as in Figure 17). The fiber ratio and l_{fiber} were kept constant at 1 mm/mm and 24.5 mm respectively.

The fiber ratio, scan amplitude, and preload, were measured through images taken in the y-z plane, as described in the scan amplitude section.

4.7.3 Results

Stability vs Length

Figure 32 displays the stability vs. the fiber ratio on the left axis and scan amplitude vs. fiber ratio on the right axis. This experiment was conducted with two different l_{fiber} lengths: 24 and 32 mm. The error bars plotted are the standard deviation of the r for 5 consecutive frames.

Both l_{fiber} lengths stability curves have a similar shape, the stability increases rapidly and then plateaus when l_{p-m} is 3/2 bigger than l_{m-t}, confirming that the stability dependence on fiber ratio is in part independent of l_{fiber}. However, once the stability plateaus at the shorter l_{fiber} the scans are consistently more stable than at the longer l_{fiber}. Also, the standard deviation is smaller so the stability reported is more precise. This is the desired

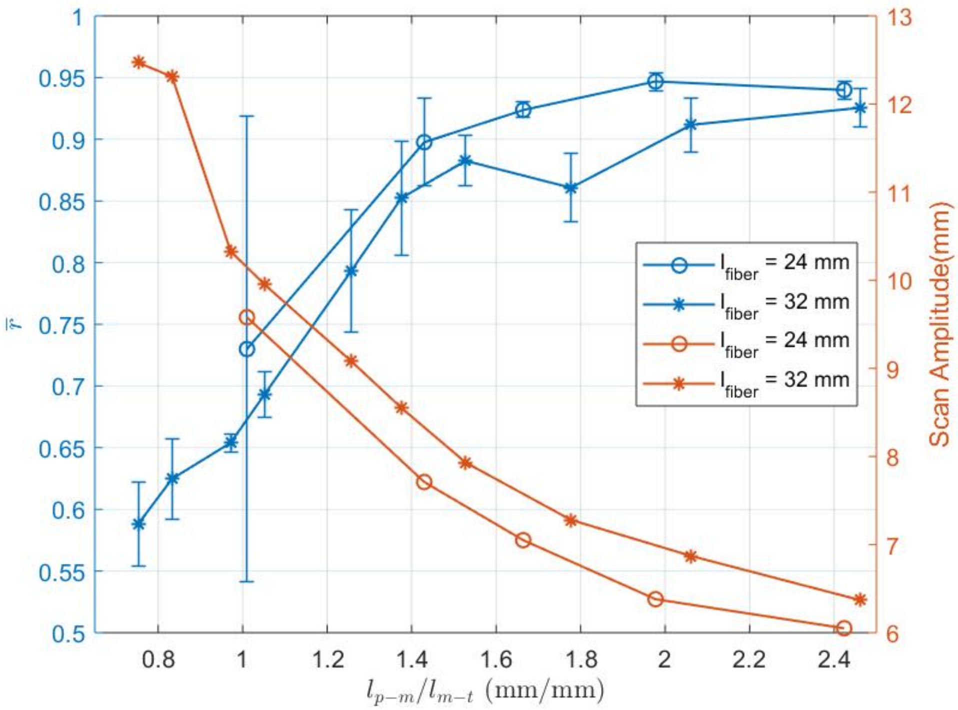

Figure 32: Left axis: stability (correlation) vs. fiber length. Right axis: Scan amplitude vs. fiber ratio at two different fiber lengths.

result, since the GEI should be as small as possible.

Furthermore, as the fiber ratio increases the scan amplitude decreases, which makes scan amplitude and stability have an inverse relationship. This is not desirable, but there are other factors, such as preload, that can be varied to improve the stability of scans at smaller fiber ratios (equivalent to larger scan amplitudes).

Stability vs Preload

Preload is critical to acquire stable scans, since it was noticed that in the cases in which there was no preload the scans would not be stable at all. Figure 33 displays the effects of having different preload on the stability of scans. The preload values reported will not have the same effect on the stability of other setups, since the stability and the preload also depend on l_{fiber} and on the fiber ratio.

From Figure 33 it can be observed that there is an optimal preload for maximum stability, however the scans are more stable when there is too much preload in comparison to too little. In the case where there is not enough preload, there is not enough force to keep

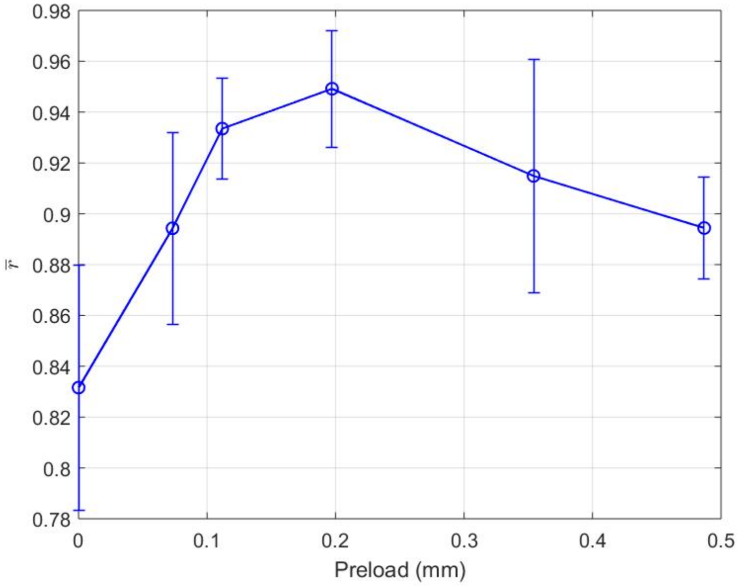

Figure 33: Stability (correlation) vs. preload with l_{fiber} 24.5 mm, scan amplitude of 9 mm, and a fiber ratio of 1.

the fiber in contact with the retaining grooves of the rotor attachment, at all times, so as the motor rotates the fibers move horizontally inside the grooves. Contrarily, when there is too much preload, the force on the motor is large and the motor does not rotate smoothly, which also results in an unstable scan.

4.8 Scan frequency

4.8.1 Background

The scan frequency (f_{scan}) was defined as the inverse of the time period between two full scans. A full scan is analogous to one full motor revolution, where for instance the fiber starts at the top, scans downwards, and then upwards back to its initial position. As per the frequency requirement f_{scan} should be of a maximum of 277 Hz in order to match the scan resolution to the optical resolution and thus not have any undersampling. The experiment performed tested how the motor's operating voltage affected the frequency, and whether the requirement could be met using the motor chosen.

4.8.2 Methodology

The frequency was measured using a photodetector (PDA100A2, Thorlabs Inc., Newton, NJ), with a 100 μm slit mounted on the front to measure each pass of the fiber in front of the detector. The detector signal was recorded using an oscilloscope. A diagram of the experimental set up is shown in Figure 34.

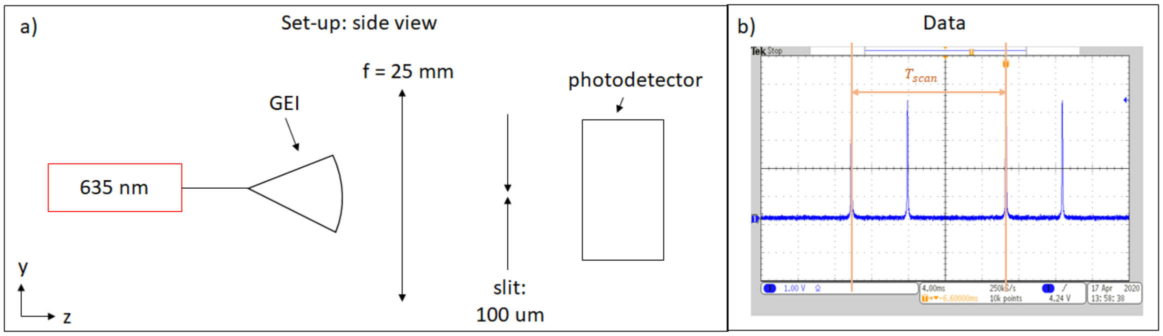

Figure 34: Frequency experimental set-up a) diagram and b) oscilloscope screenshot, from which T_{scan} was recorded for each data point.

In a full scan two signals are detected, one for the downward scan and another for the upward scan. The simplest way to measure f_{scan} was to measure the time between two downward or upward signals (i.e. every other signal detected). This measurement was more accurate because it did not depend on the phase of the scan.

The experiment performed consisted in varying the motor's operating voltage, observing whether the scan was stable and measuring the scan period (T_{scan}) using the scope. To say that the data points were stable meant that the period between the pulses was the same over a period of 5 seconds. The recorded T_{scan} value was then inverted to calculate f_{scan}.

The lower and upper bounds of the voltage range were determined by the lowest and highest voltage at which the motor would operate smoothly with the given set up.

4.8.3 Results

Figure 35 shows the effect of changing the operating voltage of the motor on f_{scan}. The point labeled with an 'x' was not stable, given that T_{scan} was not constant for 5 seconds.

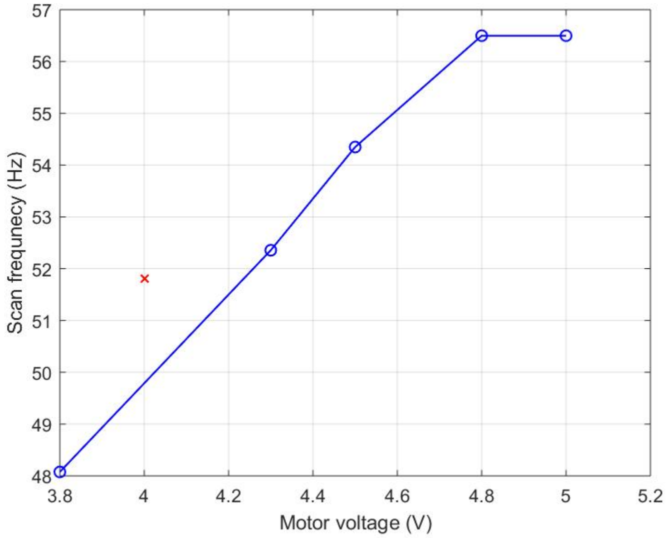

Figure 35: Scan frequency vs motor's operating voltage, point labeled with 'x' were removed because system was unstable.

As it is to be expected f_{scan} is proportional with the motor's operating voltage. At 4.8 V, the frequency of the scan plateaus, which could be because the rated voltage specified in the data sheet is in the range of 3.2 V - 4.3 V. Thus, at higher voltages the motor cannot go any faster. The slope and y-position of the curve depend on several factors, including the preload and the weight of the system. During the development of the GEI, f_{scan} was once measured to be 80 Hz when only one fiber was used.

From these results, it is evident that the system does not meet the frequency requirement specified. In order to meet the requirement the motor could be changed. The fastest DC coin motor available in Digikey was the motor W0825AB001G made by Jinlong Machinery & Electronic Co. Ltd. It is rated at 15000 rpm (250 Hz), which is faster than the motor used for this experiment rated at 12000 rpm. However a frequency of 250 Hz, will not be fast enough to meet with the scan frequency requirement of 277 Hz.

Nevertheless, a slower f_{scan} can be useful to scan the mucosa, since oversampling is necessary for vascular imaging using Doppler OCT, and could lead to enhancing the diagnostic ability of the GEI. However, the GEI would be slower at acquiring scans. For example, if the GEI was to scan at 80 Hz, it would be oversampling the image by 3.5 times. This new requirement would change the slow axis speed to 0.8 cm/s and the area scan speed to 0.72 cm^2/s, which is approximately 3 times slower than the initial requirement.

4.9 Lifetime

4.9.1 Background

The system's lifetime is defined as the time period in which the GEI is able to function consistently. There are two main components that can get damaged as the GEI operates: the motor and the fibers. It is necessary that the motor works consistently as it operates, because if it starts to slow down the scan frequency would go down and thus the scans acquired would require further work to be processed using DMDI. The fibers could be damaged in two different spots: the section in contact with the rotor attachment, or the section in contact with the pivot point. The section in contact with the rotor attachment experiences friction as the motor rotates and the section at the pivot point could potentially bend to an angle at which the fibers are being damaged as they scan. One experiment for each component was conducted.

4.9.2 Methodology

In order to test the motor's performance over time, a new motor was left scanning for 80 minutes at 4 V, and the frequency was measured at different timestamps, as detailed in the frequency section. For each data point, it was ensured that the scans were stable for 5 seconds before being recorded. During this test the system was never stopped intentionally and there were no changes made to any parameters.

For the fibers' performance, the output power of the fiber was measured against time, the system would have to be stopped for each data point taken. The power was measured using a power meter (S144C and PM100D, THORLABS Inc., Newton, NJ) and a 1310 nm laser. Only a single scanning fiber was used for testing. The fiber was not stripped of its acrylate buffer over the contact areas with the pivot point and rotor attachment. The points measured were normalized against the first measurement.

4.9.3 Results

Motor

Figure 36 shows the motor's lifetime test, it can be seen that the scan frequency of the system is approximately constant over the first 60 minutes, after which the frequency of the system decreased significantly.

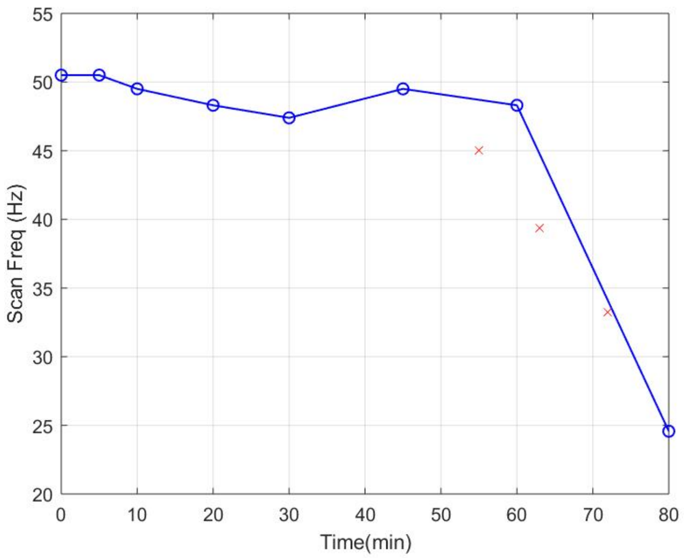

Figure 36: Motor's lifetime: frequency against time.

The points labeled with an 'x' were moments at which the motor stopped working spontaneously, and required restart. Afterwards, the motor was left running for 5 minutes in order for the scan to stabilize.

It was noted that even though the speed of the motor decreases over time if the operating voltage was increased, the motor would be able to reach the same scan frequency it had previously reached at lower voltages. Thus, it would be possible to actively monitor the speed of the scan using an optical sensor and then adjust the voltage accordingly to achieve a constant scan frequency.

The lifetime of the motor could change depending on the operating voltage of the motor, the heating of the motor, changes in friction, or wear. The lifetime may also depend on the preload and weight of the fibers.

It would also be worthwhile to perform the same test with a brushless coin motor to see if it has a longer lifetime.

Fiber

In Figure 37, results of the fibers' lifetime test is displayed. It can be seen that the power output decreases within measurement error for up to 18 hours, and afterwards it decreases to 86% of the initial power at 20 hours.

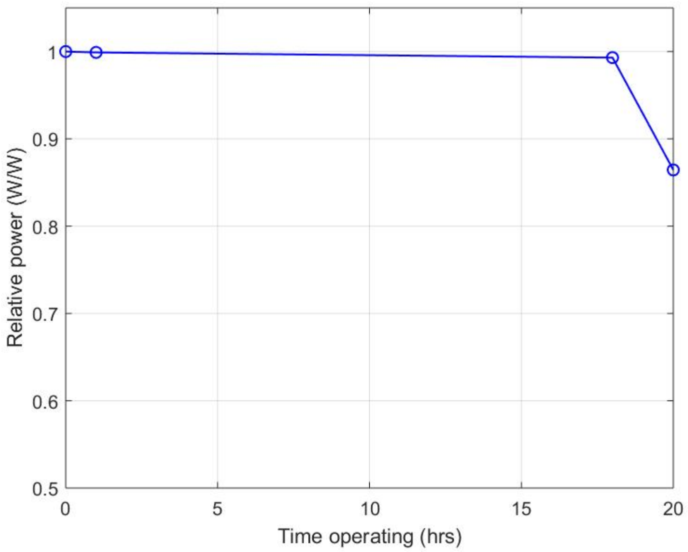

Figure 37: Fibers' lifetime test: Power output vs time.

The fibers' lifetime is not a concern since they can function properly over such a long period of time. However, the power loss, both instantaneously and over time, at the pivot point may depend on the preload of the set up. Furthermore, it was noted during testing that it is important to strip the SMF/DCFs of their acrylate as minimally as possible when cleaving them. When the acrylate was stripped until the pivot point of the scan, the fibers would easily break when being handled.

In these limited experiments, the motor and the fibers lifetime tests show that the motor and fibers will endure use during one gastroscopy. Indeed gastroscopies have an average procedure time of 5 to 15 minutes, during which the GEI will only be used for a part of this time [70].

4.10 Current State

As per the experiments performed in this section, the GEI can be built with an x and y dimension of 8 mm by 10.25 mm respectively. The GEI front area can be modelled by a rectangle with rounded edges (radius = 6 mm). Adding this rectangle to the area of the gastroscope's distal end results in a total area of 143 mm^2, which is 60 % bigger than ligators. Thus, the current state of the GEI is bigger than the size requirement. In the z-direction, a l_{fiber} of 24 mm, has been proven to acquire somewhat stable scans and achieve a scan amplitude of 9 mm, however in order to determine the GEI's total length in the z-direction the dimensions of the scan lens are also required. Lastly, the maximum f_{scan} measured with two fibers and the current set up was of 55 Hz.

4.11 Future Work

For the rotor attachment, it would be worthwhile to redesign it to be more eccentric. This would allow the system to scan larger amplitudes with smaller fibers and larger fiber ratios, resulting in more stable scans. For the housing, it is necessary to develop a system in which the angle of the fiber platform could be changed, thus adding an extra degree of freedom to the system, which would allow to explore the effects of θ_{fibers} on different characteristics of the GEI.

Finally, for product development, it is necessary to explore and design experiments that test the relationship between additional system parameters, such as: amplitude of the system vs. preload, preload vs. frequency, preload angle vs. stability.

5 Future Work

The work undertaken in this thesis project serves as the basis for developing a GEI prototype. The optical simulations will serve as guidelines on how to build the collimators to achieve the desired output beams. The mechanical system experiments allowed for the understanding of how different scanner parameters affect scan stability, frequency, and amplitude. It has been successfully demonstrated that it is feasible to develop a forward-viewing scanner using a motor-actuated fiber system. Using the current set-up, a stable scan can be obtained with a scan amplitude of at least 9 mm at a frequency of 50 Hz.

For full technical validation, the optical system needs to be built and tested with the current mechanical system, to explore the effects of having extra weight on the tips of the fibers. Additionally, the best mechanical scanner parameters to meet the requirements need to be determined. The off-axis behaviour of the optical system needs to be determined either through simulations or once it has been built. Different motors should be tested in order to pursue a higher scanning frequency. Furthermore, it may be beneficial to make the rotor attachment more eccentric to be able to acquire the same scan amplitude with shorter fibers, effectively reducing the GEI's size. It will also lead to more stable scans without sacrificing scan amplitude.

Following, an orientation test needs to be done to examine the effects of the GEI's performance when used with the different orientations. A scan calibration will be done using a printed striped pattern to determine the scan path, as previously explained in literature [5]. Following the calibration, the GEI will be tested by scanning other patterns. An image distortion simulation code will be developed, which will allow for an image processing algorithm to be adapted from similar DMDI algorithms [4]. Lastly, a GEI prototype will be built and will be used to acquire images from a pig's stomach.

5.1 Conclusion

This thesis work has shown that a forward-viewing, large FOV, scanner is realizable. Optical simulations in ZEMAX have defined how the optical collimators will be built in order to ensure gastric pits are resolvable. Additionally, several experiments were completed to understand and show that a stable scan amplitude of 9 mm is possible using a motor-actuated fiber point-scanner.

The GEI scanner will be a good enhancement to the traditional gastroscopy, it will allow for a combination of different modalities that could enhance the diagnostic process. The GEI will allow physicians to look at the stomach wall on a microscopic scale, and obtain 3-D volumes of the wall using OCT. It will also allow for high resolution images of the wall and vasculature of the stomach. The data obtained by the GEI could aid in the decision on where to take biopsies, decreasing the rate of missed diagnosis.

References

[1] J. Ferlay, I. Soerjomataram, R. Dikshit, S. Eser, C. Mathers, M. Rebelo, D. M. Parkin, D. Forman, and F. Bray, "Cancer incidence and mortality worldwide: Sources, methods and major patterns," *International Journal of Cancer*, vol. 136, no. 5, pp. E359–E386, 2015.

[2] (2019) Canadian cancer. Canadian Cancer Statistics Advisory Committee. Accessed on: 2019-06-21. [Online]. Available: cancer.ca/Canadian-Cancer-Statistics-2019-EN

[3] What happens during a gastroscopy? Institute for Quality and Efficiency in Health Care (IQWiG). Accessed on: 2020-03-30. [Online]. Available: https://www.informedhealth.org/what-happens-during-a-gastroscopy.2888.en.html

[4] M. Harlow, C. MacAulay, P. Lane, and A. Lee, "Dual-beam manually actuated distortion-corrected imaging (dmdi): two dimensional scanning with a single-axis galvanometer," *Optic Express*, vol. 26, no. 14, 2018.

[5] A. Lee, G. Hohert, M. C. P. Angkiriwang, and P. Lane, "Dual-beam manually-actuated distortion-corrected imaging (dmdi) with micromotor catheters," *Optic Express*, vol. 25, no. 16, 2017.

[6] What is stomach cancer? Canadian Cancer Society. Accessed on: 2019-06-21. [Online]. Available: http://www.cancer.ca/en/cancer-information/cancer-type/stomach/stomach-cancer/?region=on#ixzz5rVlw1rE4

[7] C. Huh, M. Bhutani, E. Farfán, and W. Bolch, "Individual variations in mucosa and total wall thickness in the stomach and rectum assessed via endoscopic ultrasound," *Physiol. Meas.*, vol. 24, no. 4, 2003.

[8] K. Yao, "Clinical application of magnifying endoscopy with narrow-band imaging in the stomach," *Clin Endosc.*, vol. 48, no. 6, pp. 481–490, Nov 2015.

[9] T. Barclay. (2020) Stomach. Innerbody. Accessed on: 2020-05-03. [Online]. Available: https://www.innerbody.com/image$_{d}igeov/dige11 - new.html$

[10] L. Tang, G. Li, Y. Sun, J. Li, and X. Zhang, "Synchrotron-radiation phase-contrast imaging of human stomach and gastric cancer: in vitro studies," *Journal of Synchrotron Radiation*, vol. 19(Part 3), no. 3, 2012.

[11] R. Ji and Y. Li, "Diagnosing helicobacter pylori infection in vivo by novel endoscopic techniques," *World J Gastroenterol.*, vol. 20, no. 28, 2014.

[12] T. Tahara, K. Takahama, N. Horiguchi, D. Yoshida, T. Kawamura, M. Okubo, T. Ishizuka, M. Nagasaka, Y. Nakagawa, T. Shibata, and N. Ohmiya, "A comparative study of magnifying blue laser imaging and magnifying narrow-band imaging system for endoscopic diagnosis of helicobacter pylori infection," *Biomedical Reports*, vol. 7, no. 3, 2017.

[13] L. Hai-Yan, G. Zhi-Zheng, F. Mitsuhiro, and L. Xiao-Bo, "Current clinical applications of magnifying endoscopy with narrow band imaging in the stomach," *Diagnostic and therapeutic endoscopy*, vol. 2012, p. 271914, 09 2012.

[14] Gastric cancer treatment (pdq®)–patient version. National Cancer Institute. Accessed on: 2019-06-26. [Online]. Available: https://www.cancer.gov/types/stomach/patient/stomach-treatment-pdq

[15] I. Vohlonen, E. Pukkala, M. H. N. Malila, M. Hakama, V. Koistinen, and P. Sipponen, "Risk of gastric cancer in helicobacter pylori infection in a 15-year follow-up," *Scandinavian Journal of Gastroenterology*, vol. 51, no. 10, 2016.

[16] What is h. pylori? WebMD. Accessed on: 2019-06-26. [Online]. Available: https://www.webmd.com/digestive-disorders/h-pylori-helicobacter-pylori#1

[17] T. Tahara, K. Takahama, N. Horiguchi, D. Yoshida, T. Kawamura, M. Okubo, T. Ishizuka, M. Nagasaka, Y. Nakagawa, T. Shibata, and N. Ohmiya, "A comparative study of magnifying blue laser imaging and magnifying narrow-band imaging system for endoscopic diagnosis of helicobacter pylori infection," *Biomedical Reports.*, vol. 7, no. 3, 2017.

[18] Intestinal metaplasia. Healthline. Accessed on: 2019-06-26. [Online]. Available: https://healthline.com/health/intestinal-metaplasia

[19] T. Almouradi, T. Hiatt, and B. Attari, "Gastric intestinal metsplasia in an underserved population in the usa: Prevalence, epidemiologic and clinical features," *Gastroenterology Research and Practice*, vol. 2013, no. 856256, 2013.

[20] L. G. Capelle, J. Haringsma, A. C. de Vries, E. W. Steyerber, K. Biermann, and H. K. E. J. van Dekken, "Narrow band imaging for the detection of gastric intestinal metaplasia

and dysplasia during surveillance endoscopy," *Digestive Diseases and Sciences*, vol. 55, no. 12, 2010.

[21] Y. Zhu, F. Wang, Y. Zhou, G. L. Xi, L. Dong, W. H. He, and B. Xiao, "Blue laser magnifying endoscopy in the diagnosis of chronic gastritis," *Exp Ther Med.*, vol. 18, no. 3, 2019.

[22] J.-W. Kim, "Usefulness of narrow-band imaging in endoscopic submucosal dissection of the stomach," *Clin Endosc.*, vol. 51, no. 6, 2018.

[23] J. Lee, L. G. Lim, and K. G. Yeoh, "Advanced endoscopic imaging in gastric neoplasia and preneoplasia," *BMJ Open Gastroenterol*, vol. 4, no. 1, 2017.

[24] S. A. Taghavi, M. M. Ebrahim, A. Eshraghian, S. D. Moshen, L. Hamidpour, and F. Khademalhoseini, "Comparison of chromoendoscopy and conventional endoscopy in the detection of premalignant gastric lesions," *Canadian Journal of Gastroenterology*, vol. 23, no. 2, 2009.

[25] M. Dinis-Ribeiro, A. da Costa-Pereira, C. Lopes, L. Lara-Santos, M. Guilherme, L. Moreira-Dias, H. Lomba-Viana, and A. Ribeiro, "Magnification chromoendoscopy for the diagnosis of gastric intestinal metaplasia and dysplasia," *Gastrointestinal Endoscopy*, vol. 14, no. 57, 2003.

[26] Products: Gif-hq290. Olympus. Accessed on: 2020-05-13. [Online]. Available: https://www.olympus.co.uk/medical/en/Products-and-solutions/Products/Product/GIF-HQ290.html

[27] P. Trivedi and B. Braden, "Indications, stains and techniques in chromoendoscopy," *QJM*, vol. 106, no. 2, 2013.

[28] J. Picot, M. Rose, and K. Cooper, *Virtual chromoendoscopy for the real-time assessment of colorectal polyps in vivo: a systematic review and economic evaluation.* Southampton, UK: NIHR Journals Library, 2017.

[29] Y. Ezoe, M. Muto, N. Uedo, H. Doyama, L. Yao, I. Oda, K. Kaneko, Y. Kawahara, C. Yokoi, Y. Sugiura, H. Ishikawa, Y. T. andY. Kaneko, and Y. Saito, "Magnifying narrowband imaging is more accurate than conventional white-light imaging in diagnosis of gastric mucosal cancer," *Gastroenterology*, vol. 141, no. 6, 2011.

[30] L. G. Capelle, J. Haringsma, A. C. de Vries, E. W. Steyerberg, K. Biermann, H. van Dekken, and E. J. Kuipers, "Narrow band imaging for the detection of gastric intestinal metaplasia and dysplasia during surveillance endoscopy," *Dig Dis Sci.*, vol. 55, no. 12, 2010.

[31] N. Horiguchi, T. Tahara, T. Kawamura, M. Okubo, S. Tahara, M. Nagasaka, Y. Nakagawa, T. Shibata, and N. Ohmiya, "A comparative study of white light endoscopy, chromoendoscopy and magnifying endoscopy with narrow band imaging in the diagnosis of early gastric cancer after helicobacter pylori eradication." *J Gastrointestin Liver Dis.*, vol. 26, no. 4, 2017.

[32] S. Barbeiro, D. Libânio, C. Dinis-Ribeiro, and P. Pimentel-Nunes, "Narrow-band imaging: Clinical application in gastrointestinal endoscopy," *Portuguese Journal of Gastroenterology*, vol. 2019, no. 26, 2019.

[33] O. Dohi, N. Yagi, A. Majima, Y. Horii, T. Kitaichi, Y. Onozawa, K. Suzuki, A. Tomie, R. Kimura-Tsuchiya, T. Tsuji, N. Yamada, N. Bito, T. Okayama, N. Yoshida, K. Kamada, K. Katada, K. Uchiyama, T. Ishikawa, T. Takagi, O. Handa, H. Konishi, Y. Naito, A. Yanagisawa, and Y. Itoh, "Diagnostic ability of magnifying endoscopy with blue laser imaging for early gastric cancer: a prospective study," *Gastric Cancer*, vol. 20, no. 2, 2017.

[34] K. Kaneko, Y. Oono, T. Yano, T. O. H. Ikematsu, Y. Yoda, A. Yagishita, A. Sato, and S. Nomura, "Effect of novel bright image enhanced endoscopy using blue laser imaging (bli)," *Endoscopy Int Open*, vol. 2, no. 4, 2014.

[35] T. Fujiyoshi, R. Miyahara, K. F. Kohei Funasaka and, T. Sawada, K. Maeda, T. Yamamura, T. Ishikawa, E. Ohno, M. Nakamura, H. Kawashima, M. Nakaguro, M. Nakatochi, and Y. Hirooka, "Utility of linked color imaging for endoscopic diagnosis of early gastric cancer," *World J Gastroenterol.*, vol. 25, no. 10, 2019.

[36] H. Osawa, Y. Miura, T. Takezawa, Y. Ino, T. Khurelbaatar, Y. Sagara, A. K. Lefor, and H. Yamamoto, "Linked color imaging and blue laser imaging for upper gastrointestinal screening," *Clin Endosc.*, vol. 51, no. 6, 2018.

[37] Lasereo: L580series. Fujifilm. Accessed on: 2020-05-13. [Online]. Available: https://www.fujifilm.com/products/medical/endoscopy/lasereo/specifications3

[38] A. Nakano, Y. Hirooka, T. Yamamura, O. Watanabe, M. Nakamura, K. Funasaka, E. Ohno, H. Kawashima, R. Miyahara, and H. Goto, "Comparison of the diagnostic ability of blue laser imaging magnification versus pit pattern analysis for colorectal polyps," *Endosc Int Open.*, vol. 5, no. 4, 2017.

[39] O. Dohi, N. Yagi, Y. Onozawa, R. Kimura-Tsuchiya, A. Majima, T. Kitaichi, Y. Horii, K. Suzuki, A. Tomie, T. Okayama, N. Yoshida, K. Kamada, K. Katada, K. Uchiyama, T. Ishikawa, T. Takagi, O. Handa, H. Konishi, Y. Naito, and Y. Itoh, "Linked color imaging improves endoscopic diagnosis of active helicobacter pylori infection," *Endosc Int Open.*, vol. 4, no. 7, 2016.

[40] Eg-760z: Specifications. Fujifilm. Accessed on: 2020-05-13. [Online]. Available: https://www.fujifilm.eu/eu/products/medical-systems/endoscopy/endoscopy-products/p/eg-760zoverview

[41] K. Kobayashi, R. Miyahara, K. Funasaka, K. Furukawa, T. Sawada, K. Maeda, T. Yamamura, T. Ishikawa, E. Ohno, M. Nakamura, H. Kawashima, M. Nakaguro, Y. Okumura, Y. Hirooka, and M. Fujishiro, "Color information from linked color imaging is associated with invasion depth and vascular diameter in superficial esophageal squamous cell carcinoma," *Japan Gastroenterological Endoscopy Society*, vol. 32, no. 1, 2019.

[42] H. Pahlevaninezhad, A. Lee, A. Ritchie, T. Shaipanich, W. Zhang, D. N. Ionescu, G. Hohert, C. MacAulay, S. Lam, and P. Lane, "Endoscopic doppler optical coherence tomography and autofluorescence imaging of peripheral pulmonary nodules and vasculature," *Biomedical Optics Express*, vol. 6, no. 10, 2015.

[43] M. Kato, M. Kaise, J. Yonezawa, Y. Yoshida, and H. Tajiri, "Autofluorescence endoscopy versus conventional white light endoscopy for the detection of superficial gastric neoplasia: a prospective comparative study," *Endoscopy*, vol. 39, no. 11, 2007.

[44] (2007, 01) Olympus introduces phase 2 of its evis lucera gastrointestinal tract endoscopy system for observation using specific light spectra world's first gastrointestinal videoscopes with auto fluorescence imaging capability -evis lucera gastrointestinal videoscope gif type fq260z- evis lucera colonovideoscope cf type fh260az series. Olympus. Accessed on: 2020-05-13. [Online]. Available: https://www.olympus-global.com/en/news/2007a/nr070117evise.html

[45] A. Fugazza, F. Gaiani, M. C. Carra, F. Brunetti, M. Lévy, I. Sobhani, D. Azoulay, F. Catena, G. L. de'Angelis, and N. de'Angelis, "Confocal laser endomicroscopy in gastrointestinal and pancreatobiliary diseases: A systematic review and meta-analysis," *Biomed Res Int*, vol. 2016, no. 4638683, 2016.

[46] T. Adam and J. H. Hwang, "Confocal microscopy in the esophagus and stomach," *Clinical Endoscopy*, vol. 46, no. 5, 2013.

[47] W. J. Choi and R. K. Wang, "Swept-source optical coherence tomography powered by a 1.3-μm vertical cavity surface emitting laser enables 2.3-mm-deep brain imaging in mice in vivo," *J Biomed Opt*, vol. 20, no. 10, 2015.

[48] D. Popescu, L. Choo-Smith, C. Flueraru, Y. Mao, S. Chang, J. Disano, S. Sherif, and M. Sowa, "Optical coherence tomography: fundamental principles, instrumental designs and biomedical applications," *Biophysical Reviews*, vol. 3, no. 115, 2011.

[49] D. Huang, E. A. Swanson, C. P. Lin, J. S. Schuman, W. G. Stinson, W. Chang, T. F. M. R. Hee, K. Gregory, C. A. Puliafito, and J. G. Fujimoto, "Optical coherence tomography," *Science*, vol. 254, no. 5035, 1991.

[50] W. O'Brien, "Single-element transducers," *Radiographics*, no. 13, 1993.

[51] T. Rösch, "Endoscopic ultrasonography: imaging and beyond," *Gut*, vol. 52, no. 8, 2003.

[52] A. Chung and V. Kwancorresponding, "Endoscopic ultrasound: an overview of its role in current clinical practice," *Australas J Ultrasound Med.*, vol. 12, no. 2, 2009.

[53] T. Tsai, C. L. Leggett, A. J. Trindade, A. Sethi, A. Swager, V. Joshi, J. J. Bergman, H. Mashimo, N. S. Nishioka, and E. Namati, "Optical coherence tomography in gastroenterology: a review and future outlook," *Journal of Biomedical Optics*, vol. 22, no. 12, 2017.

[54] M. M. Xu, S. M. Lagana, and A. Sethi, "Use of optical coherence tomography (oct) in the evaluation of gastric lesions," *Gastrointestinal Endoscopy*, vol. 81, no. 5, 2015.

[55] K. Yao, *Zoom Gastroscopy: Magnifying Endoscopy in the Stomach.* Springer Science Business Media, 2013.

[56] (2017, 12) Tests for stomach cancer. American Cancer Society. Accessed on: 2019-07-22. [Online]. Available: https://www.cancer.org/cancer/stomach-cancer/detection-diagnosis-staging.html

[57] A. Peixoto, M. Silva, P. Pereira, and G. Macedo, “Biopsies in gastrointestinal endoscopy: When and how,” *Port J Gastroenterol.*, vol. 23, no. 1, 2016.

[58] S. Menon and N. Trudgill, “How commonly is upper gastrointestinal cancer missed at endoscopy? a meta-analysis,” *Endoscopoy International Open*, vol. 2, 2014.

[59] A. De-Vries, J. Haringsma, R. De-Vries, F. Ter-Borg, N. Van-Grieken, G. Meijer, H. Van-Dekken, and E. Kuipers, “Biopsy strategies for endoscopic surveillance of pre-malignant gastric lesions,” *Helicobacter*, vol. 15, no. 4, 2010.

[60] A. M. Sergeev, V. M. Gelikonov, G. Gelikonov, F. I. Feldchtein, R. V. Kuranov, N. D. Gladkova, N. M. Shakhova, L. B. Snopova, A. V. Shakhov, I. A. Kuznetzova, A. N. Denisenko, V. V. Pochinko, and Y. P. Chumakov, “In vivo endoscopic oct imaging of precancer and cancer states of human mucosa,” *Opt. Express*, vol. 1, no. 13, 1997.

[61] A. Lee, L. Cahill, K. Liu, C. MacAulay, C. Poh, and P. Lane, “Wide-field in vivo oral oct imaging.” *Biomed Opt Express.*, vol. 6, no. 7, 2015.

[62] E. J. Seibel and Q. Y. J. Smithwick, “Unique features of optical scanning, single fiber endoscopy,” *Lasers in Surgery and Medicine*, vol. 30, no. 3, 2002.

[63] T. Xie, H. Xie, G. K. Fedder, and Y. Pan, “Endoscopic optical coherence tomography with a modified microelectromechanical systems mirror for detection of bladder cancers,” *Optics Express*, vol. 42, no. 31, 2003.

[64] T. Wu, Z. Ding, K. Wang, M. Chen, and C. Wang, “Two-dimensional scanning realized by an asymmetry fiber cantilever driven by single piezo bender actuator for optical coherence tomography,” *Optics Express*, vol. 17, no. 16, 2009.

[65] S. Moon, S. Lee, M. Rubinstein, B. J. F. Wong, and C. Zhongping, “Semi-resonant operation of a fiber-cantilever piezotube scanner for stable optical coherence tomography endoscope imaging,” *Optics Express*, vol. 18, no. 20, 2010.

[66] A. L. Buenconsejo, G. Hohert, M. Manning, E. Abouei, R. Tingley, I. Janzen, J. McAlpine, D. Miller, A. Lee, P. Lane, and C. MacAulay, “Submillimeter diameter rotary-pullback fiber-optic endoscope for narrowband red-green-blue reflectance, optical coherence tomography, and autofluorescence in vivo imaging,” *J. of Biomedical Optics*, vol. 25, no. 3, 2019.

[67] (2004) Power budgets and loss budgets. Power Budgets And Loss Budgets. Accessed on: 2020-03-15. [Online]. Available: https://www.thefoa.org/tech/lossbudg.htm

[68] S. Lemire-Renaud, M. Rivard, D. M. M. Strupler, F. Verpillat, X. Daxhelet, N. Godbout, and C. Boudoux, "Double-clad fiber coupler for endoscopy," *Opt. Express*, vol. 18, no. 10, 2010.

[69] J. L. Vazques-Iglesias, P. A. Alonso-Aguirre, A. Centeno, E. Lopez, R. T., and S. Blanco, "Perforation risk in esophageal endoscopic mucosal resection with ligation: an experimental study with two ligator models," *Revista espanola de enfermedades digestivas*, vol. 99, no. 2, 2007.

[70] Services:endoscopy: Frequently asked questions. Cambridge University Hospitals. Accessed on: 2019-04-14. [Online]. Available: https://www.cuh.nhs.uk/addenbrookes-hospital/services/endoscopy/faqs

Appendix

Gastroscopes' resolution and FOV

Gastroscopes' FOV is usually reported in degrees. Thus, to convert it to an area space (mm^2), and make it comparable to how the GEI's FOV is reported, it is necessary to select the focal distance at which it is used. In the case of the maximum resolution, the minimum focal distance reported in the specification sheet was used, and it was assumed that the gastroscopes' FOV are circular. This distance and the FOV in degrees was used to find the radius of the FOV in mm, through a tangent operation, using the set-up in Figure 38.

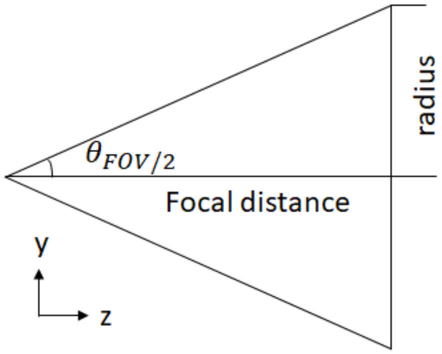

Figure 38: Set-up used to calculate FOV of endoscope in mm. θ_{FOV} is the reported FOV in degrees divided by two.

To find the resolution, the diameter of the circular FOV is divided by the resolution specified in the specification sheet (i.e.: HD = 10080 px)

ZEMAX screenshots

Below there are screenshots of ZEMAX's merit function and set-up of non-sequential system.

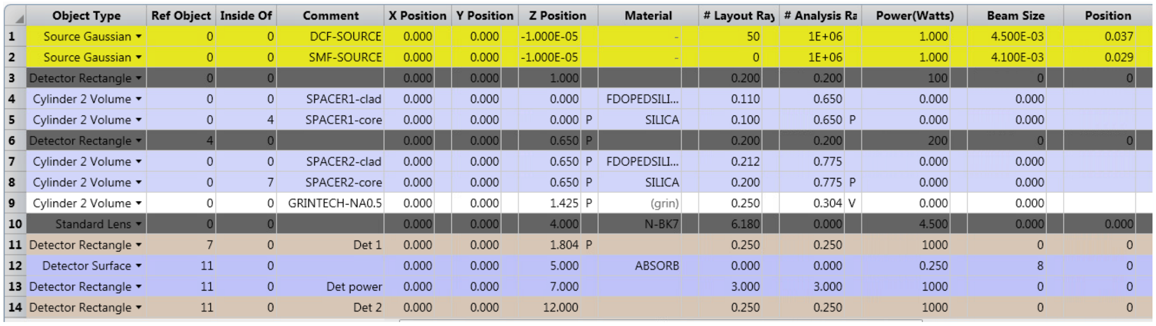

	Object Type	Ref Object	Inside Of	Comment	X Position	Y Position	Z Position	Material	# Layout Ray	# Analysis Ra	Power(Watts)	Beam Size	Position
1	Source Gaussian	0	0	DCF-SOURCE	0.000	0.000	-1.000E-05	-	50	1E+06	1.000	4.500E-03	0.037
2	Source Gaussian	0	0	SMF-SOURCE	0.000	0.000	-1.000E-05	-	0	1E+06	1.000	4.100E-03	0.029
3	Detector Rectangle	0	0		0.000	0.000	1.000		0.200	0.200	100	0	0
4	Cylinder 2 Volume	0	0	SPACER1-clad	0.000	0.000	0.000	FDOPEDSILI...	0.110	0.650	0.000	0.000	
5	Cylinder 2 Volume	0	4	SPACER1-core	0.000	0.000	0.000 P	SILICA	0.100	0.650 P	0.000	0.000	
6	Detector Rectangle	4	0		0.000	0.000	0.650 P		0.200	0.200	200	0	0
7	Cylinder 2 Volume	0	0	SPACER2-clad	0.000	0.000	0.650 P	FDOPEDSILI...	0.212	0.775	0.000	0.000	
8	Cylinder 2 Volume	0	7	SPACER2-core	0.000	0.000	0.650 P	SILICA	0.200	0.775 P	0.000	0.000	
9	Cylinder 2 Volume	0	0	GRINTECH-NA0.5	0.000	0.000	1.425 P	(grin)	0.250	0.304 V	0.000	0.000	
10	Standard Lens	0	0		0.000	0.000	4.000	N-BK7	6.180	0.000	4.500	0.000	0.000
11	Detector Rectangle	7	0	Det 1	0.000	0.000	1.804 P		0.250	0.250	1000	0	0
12	Detector Surface	11	0		0.000	0.000	5.000	ABSORB	0.000	0.000	0.250	8	0
13	Detector Rectangle	11	0	Det power	0.000	0.000	7.000		3.000	3.000	1000	0	0
14	Detector Rectangle	11	0	Det 2	0.000	0.000	12.000		0.250	0.250	1000	0	0

Figure 39: Non-sequential editor used for optical simulations. Column names correspond to the light sources (row 1 and 2)

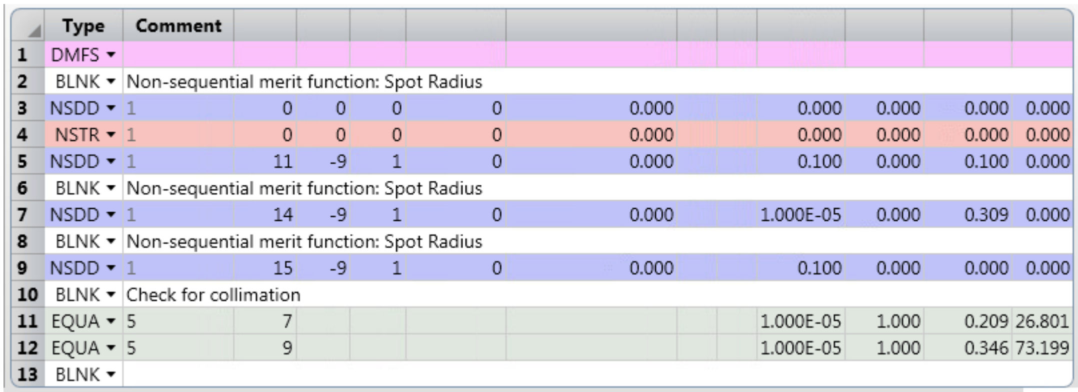

	Type	Comment											
1	DMFS												
2	BLNK	Non-sequential merit function: Spot Radius											
3	NSDD	1	0	0	0	0	0.000			0.000	0.000	0.000	0.000
4	NSTR	1	0	0	0	0	0.000			0.000	0.000	0.000	0.000
5	NSDD	1	11	-9	1	0	0.000			0.100	0.000	0.100	0.000
6	BLNK	Non-sequential merit function: Spot Radius											
7	NSDD	1	14	-9	1	0	0.000			1.000E-05	0.000	0.309	0.000
8	BLNK	Non-sequential merit function: Spot Radius											
9	NSDD	1	15	-9	1	0	0.000			0.100	0.000	0.000	0.000
10	BLNK	Check for collimation											
11	EQUA	5	7							1.000E-05	1.000	0.209	26.801
12	EQUA	5	9							1.000E-05	1.000	0.346	73.199
13	BLNK												

Figure 40: Merit function used to find GRIN vs MMF parameters in Figure 10